



# Examining Pathways of Iron and Sulfur Acquisition, Trafficking, Deployment, and Storage in Mineral-Grown Methanogen Cells

Devon Payne,<sup>a</sup> Eric M. Shepard,<sup>b</sup>  Rachel L. Spietz,<sup>a</sup> Katherine Steward,<sup>b</sup> Sue Brumfield,<sup>c</sup> Mark Young,<sup>c</sup>  Brian Bothner,<sup>b</sup> William E. Broderick,<sup>b</sup> Joan B. Broderick,<sup>b</sup>  Eric S. Boyd<sup>a</sup>

<sup>a</sup>Department of Microbiology and Immunology, Montana State University, Bozeman, Montana, USA

<sup>b</sup>Department of Chemistry and Biochemistry, Montana State University, Bozeman, Montana, USA

<sup>c</sup>Department of Plant Sciences, Montana State University, Bozeman, Montana, USA

**ABSTRACT** Methanogens have a high demand for iron (Fe) and sulfur (S); however, little is known of how they acquire, deploy, and store these elements and how this, in turn, affects their physiology. Methanogens were recently shown to reduce pyrite (FeS<sub>2</sub>), generating aqueous iron sulfide (FeS<sub>aq</sub>) clusters that are likely assimilated as a source of Fe and S. Here, we compared the phenotypes of *Methanococcus voltae* grown with FeS<sub>2</sub> or ferrous iron [Fe(II)] and sulfide (HS<sup>-</sup>). FeS<sub>2</sub>-grown cells are 33% smaller yet have 193% more Fe than Fe(II)/HS<sup>-</sup>-grown cells. Whole-cell electron paramagnetic resonance revealed similar distributions of paramagnetic Fe, although FeS<sub>2</sub>-grown cells showed a broad spectral feature attributed to intracellular thioferrate-like nanoparticles. Differential proteomic analyses showed similar expression of core methanogenesis enzymes, indicating that Fe and S source does not substantively alter the energy metabolism of cells. However, a homolog of the Fe(II) transporter FeoB and its putative transcriptional regulator DtxR were up-expressed in FeS<sub>2</sub>-grown cells, suggesting that cells sense Fe(II) limitation. Two homologs of IssA, a protein putatively involved in coordinating thioferrate nanoparticles, were also up-expressed in FeS<sub>2</sub>-grown cells. We interpret these data to indicate that, in FeS<sub>2</sub>-grown cells, DtxR cannot sense Fe(II) and therefore cannot downregulate FeoB. We suggest this is due to the transport of Fe(II) complexed with sulfide (FeS<sub>aq</sub>), leading to excess Fe that is sequestered by IssA as a thioferrate-like species. This model provides a framework for the design of targeted experiments aimed at further characterizing Fe acquisition and homeostasis in *M. voltae* and other methanogens.

**IMPORTANCE** FeS<sub>2</sub> is the most abundant sulfide mineral in the Earth's crust and is common in environments inhabited by methanogenic archaea. FeS<sub>2</sub> can be reduced by methanogens, yielding aqueous FeS<sub>aq</sub> clusters that are thought to be a source of Fe and S. Here, we show that growth of *Methanococcus voltae* on FeS<sub>2</sub> results in smaller cell size and higher Fe content per cell, with Fe likely stored intracellularly as thioferrate-like nanoparticles. Fe(II) transporters and storage proteins were upregulated in FeS<sub>2</sub>-grown cells. These responses are interpreted to result from cells incorrectly sensing Fe(II) limitation due to assimilation of Fe(II) as FeS<sub>aq</sub>. These findings have implications for our understanding of how Fe/S availability influences methanogen physiology and the biogeochemical cycling of these elements.

**KEYWORDS** methanogen, iron-sulfur cluster, proteomics, FeS<sub>2</sub>, pyrite, mackinawite, FeS, DtxR, EPR, Feo

**M**ethanogens, organisms that generate methane (CH<sub>4</sub>) from carbon dioxide (CO<sub>2</sub>) and hydrogen (H<sub>2</sub>) and/or small organic molecules such as acetate, formate, and methanol, play key roles in the biogeochemical cycling of elements (1). Methanogens are also models for numerous biofuel applications, including as feedstocks of CH<sub>4</sub> and other compounds (e.g., H<sub>2</sub>) that could be used as alternatives to fossil crude oil and

**Citation** Payne D, Shepard EM, Spietz RL, Steward K, Brumfield S, Young M, Bothner B, Broderick WE, Broderick JB, Boyd ES. 2021. Examining pathways of iron and sulfur acquisition, trafficking, deployment, and storage in mineral-grown methanogen cells. *J Bacteriol* 203:e00146-21. <https://doi.org/10.1128/JB.00146-21>.

**Editor** Michael Y. Galperin, NCBI, NLM, National Institutes of Health

**Copyright** © 2021 Payne et al. This is an open-access article distributed under the terms of the [Creative Commons Attribution 4.0 International license](https://creativecommons.org/licenses/by/4.0/).

Address correspondence to Eric S. Boyd, [eric.boyd@montana.edu](mailto:eric.boyd@montana.edu).

**Received** 15 March 2021

**Accepted** 5 July 2021

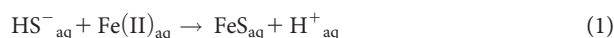
**Accepted manuscript posted online** 12 July 2021

**Published** 8 September 2021

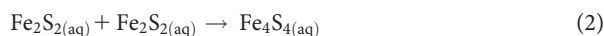
natural gas as energy storage molecules (2). Much of the impact of methanogens on biogeochemical cycles and their utility as production platforms for energy storage molecules is attributable to the abundance and diversity of metalloproteins that support their cellular energy metabolism (1). The functioning of these metalloproteins is often dependent on both simple and complex iron-sulfur ([Fe-S]) clusters that are involved in electron transfer as well as substrate binding, activation, and catalysis (3, 4). This includes metalloproteins involved in the interconversion of H<sub>2</sub> ([NiFe] hydrogenase), reduction of dinitrogen to ammonia (nitrogenase), and interconversion of carbon monoxide and CO<sub>2</sub> (carbon monoxide dehydrogenase) (1, 5–7).

The dependence of methanogen metabolism on simple and complex [Fe-S] clusters is underscored by several recent studies that showed that methanogens have a large demand for Fe and S relative to other cell types (8–10). For example, *Methanococcus maripaludis* cells contained ~15-fold more [Fe-S] clusters per mg protein than *Escherichia coli* cells (9), and the inferred proteomes of several model methanogens code for a higher number of [Fe-S] cluster binding motifs than those of facultative and obligate aerobes (10). Further, a recent analysis of >300 archaeal methanogen genomes found that roughly 5 to 8% of the total encoded proteins are predicted to bind [Fe-S] clusters (8). The greater reliance on [Fe-S] clusters in methanogen cells relative to other facultatively anaerobic or aerobic cells has been suggested to result from increased bioavailability of Fe and S in the anoxic early Earth environments (11), when the primary diversification of this group of organisms is thought to have taken place, >3.51 giga-annums (Ga) ago (12).

Contemporary methanogens typically inhabit euxinic environments that are rich in sulfide (HS<sup>-</sup>) and reduced metals, including Fe(II) (1). Sulfide readily reacts with metals such as Fe(II) (equation 1) and other trace metals [e.g., Ni(II), Co(II), and Zn(II)] to form precipitates with limited solubility (13).



In the case of Fe(II), reaction with HS<sup>-</sup> initially yields soluble iron monosulfide clusters (FeS<sub>aq</sub>) (equation 1) (14) that can nucleate to form soluble nanoparticles with stoichiometries of up to Fe<sub>150</sub>S<sub>150(aq)</sub> (equation 2).



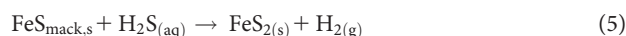
FeS<sub>aq</sub> nanoparticles containing >150 FeS units precipitate as iron sulfide (FeS) solid phases such as mackinawite (FeS<sub>mack</sub>) (equation 3) (15).



Oxidation of FeS<sub>mack</sub> by sulfur compounds of intermediate oxidation state, such as polysulfide or elemental sulfur (S<sup>0</sup>), yields pyrite (FeS<sub>2</sub>) (equation 4) (16–19).



It has also been suggested that FeS<sub>mack</sub> can be oxidized by H<sub>2</sub>S to form FeS<sub>2</sub> (equation 5) (20, 21).



FeS<sub>aq</sub>, FeS<sub>mack</sub>, and FeS<sub>2</sub> are common in anoxic, sulfidic environments inhabited by methanogens (reviewed in references 15 and 21), and as previously mentioned, their formation proceeds via soluble (hydrated) molecular FeS<sub>aq</sub> cluster intermediates (e.g., Fe<sub>2</sub>S<sub>2</sub> · 4H<sub>2</sub>O) that are small (<2 nm; <150 FeS units) (18). Thermodynamic modeling indicates that the dominant form of FeS<sub>aq</sub> at circumneutral to slightly alkaline pH is the uncharged FeS<sup>0</sup><sub>aq</sub> species, while protonated FeHS<sup>+</sup><sub>aq</sub> species predominate at slightly acidic pH (<6.5) (15, 22). This opens the possibility that small, dissolved, and uncharged FeS<sup>0</sup><sub>aq</sub> molecular clusters could theoretically diffuse across the cell membrane or, if present as charged

clusters ( $\text{FeHS}_{\text{aq}}^+$ ), be actively transported into cells at physiological pH. Alternatively, protein- or ligand-bound  $\text{FeS}_{\text{aq}}$  clusters could be transported into cells. Once inside the cells, FeS species could be trafficked via unknown mechanisms to meet the Fe and/or S demands associated with biosynthesis of amino acids, vitamins, [Fe-S] clusters, and other cofactors (e.g., siroheme) or coenzymes (e.g., coenzyme M [CoM]).

Recent data show that *Methanococcus voltae* A3 and *Methanosarcina barkeri* MS, representatives of early diverging hydrogenotrophic methanogens that lack cytochromes and more recently diverging methanogens that possess cytochromes (23–25), respectively, can reductively dissolve  $\text{FeS}_2$  and use released Fe and S to meet biosynthetic demands (26). Interestingly, during reduction of  $\text{FeS}_2$ ,  $\text{HS}^-$  was found to be released into the aqueous phase; however, Fe(II) was not detectable in solution. Further, addition of 1 mM  $\text{HS}^-$  to cultures grown with  $\text{FeS}_2$  had no impact on growth kinetics, and instead, cells continued to produce  $\text{HS}^-$  through reduction of  $\text{FeS}_2$ . This indicates that  $\text{HS}^-$  is unlikely to be the primary source of S that is assimilated in cells that are reducing  $\text{FeS}_2$ .

Previous abiotic studies conducted at high temperature ( $>90^\circ\text{C}$ ) and high  $\text{H}_2$  partial pressure ( $>8 \times 10^5$  Pa) have shown that reductive dissolution of  $\text{FeS}_2$  (reverse of equation 4) occurs through a coupled dissolution/precipitation process, with an FeS phase most likely to be pyrrhotite ( $\text{Fe}_{1-x}\text{S}_{\text{pyr}}$ ) forming on the surface of  $\text{FeS}_2$  (27).  $\text{FeS}_{\text{mack}}$  and  $\text{Fe}_{1-x}\text{S}_{\text{pyr}}$  are slightly soluble (solubility product =  $10^{-35}$ , contingent on the availability of  $\text{HS}^-$  [15]), and it is possible that surface-associated FeS (either  $\text{FeS}_{\text{mack}}$  or  $\text{Fe}_{1-x}\text{S}_{\text{pyr}}$ ) dissolves and establishes an equilibrium with the aqueous phase as  $\text{FeS}_{\text{aq}}$ , which could be the species cells use to simultaneously meet Fe and S demands. In particular, in the presence of  $>1 \mu\text{M}$   $\text{HS}^-$ , as is the case in cultures of *M. voltae* or *M. barkeri* grown with  $\text{FeS}_2$  as the sole Fe and S source, the predominant form of Fe(II) in equilibrium with  $\text{FeS}_{\text{mack}}$  approaches  $1 \mu\text{M}$  as  $\text{FeS}_{\text{aq}}$  species (15). The concentration of  $\text{HS}^-$  in the medium of *M. voltae* and *M. barkeri* cultures growing with  $\text{FeS}_2$  ranges from 5 to  $30 \mu\text{M}$  (26), well above the  $1 \mu\text{M}$  threshold level needed to stabilize the predominant form of Fe(II) in solution as  $\text{FeS}_{\text{aq}}$ . Previous studies have also suggested the possibility that  $\text{FeS}_{\text{aq}}$  is the form of Fe and S assimilated by methanogens (28). Nonetheless, it is not clear what the consequences of potential assimilation of Fe and S (as  $\text{FeS}_{\text{aq}}$ ) at an ~1:1 stoichiometric ratio may be, given that cells need more S than they do Fe (9). Further, it is unknown whether cells acclimate to use less Fe or S when grown with mineral sources of Fe/S compared to growth with Fe(II)/ $\text{HS}^-$  and whether this, in turn, alters the distribution of Fe and S in cells. Addressing such questions has consequences for understanding the sources and sinks of Fe and S in euxinic environments inhabited by methanogens and could provide new insights into potential limitations imposed by Fe and S availability and speciation on the activity and function of such cells in natural systems.

In the present study, we examined *M. voltae* A3 cells grown with formate in minimal base salts medium provided with either Fe(II)/ $\text{HS}^-$  or  $\text{FeS}_2$  as the sole source of Fe and S. Electron microscopy was used to identify morphological differences between cells. Cells were analyzed for differences in cellular Fe content using atomic absorption (AA) spectroscopy and were examined for variation in the abundance and composition of [Fe-S] clusters using electron paramagnetic resonance (EPR) spectroscopy. Finally, cells were subjected to differential proteomics analyses to identify similarities and differences in the abundances of proteins involved in core methanogenesis pathways, those involved in Fe acquisition/homeostasis, and those that bind [Fe-S] clusters as indicators of potential changes in energy metabolism, Fe/S acquisition, and Fe/S deployment, respectively. Results are discussed in terms of potential pathways for assimilating  $\text{FeS}_{\text{aq}}$  and the consequences for growth with soluble versus mineral forms of Fe and S in terms of sources and sinks of Fe and S.

## RESULTS AND DISCUSSION

**Cell morphology and size.** Cultures of *M. voltae* grown with formate as the electron donor and provided with either Fe(II)/ $\text{HS}^-$  or  $\text{FeS}_2$  as the sole Fe and S source were examined using transmission electron microscopy (TEM). While the overall shape of cells did not differ substantively between treatments (i.e., all were irregular, elongated coccoids), clear differences were observed in the size of cells, with Fe(II)/ $\text{HS}^-$ - and  $\text{FeS}_2$ -grown cells being roughly

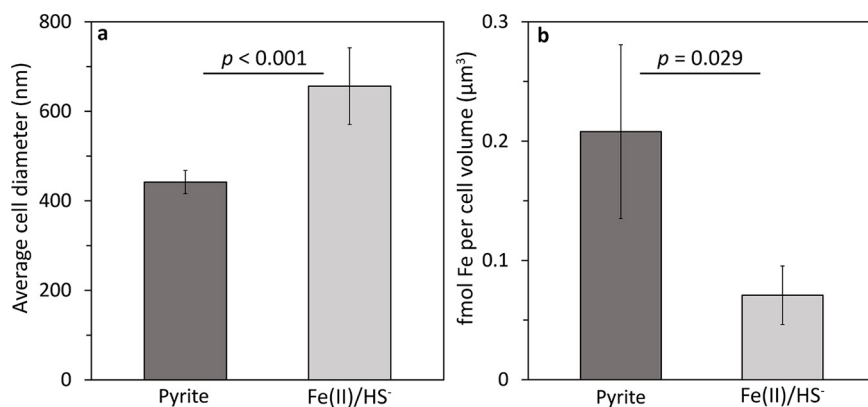


**FIG 1** Cell size and iron (Fe) content of *Methanococcus voltae* grown with different Fe and sulfur (S) sources. *M. voltae* was grown in base salts medium with either synthetic pyrite nanoparticles or ferrous iron [Fe(II)] and sulfide (HS<sup>-</sup>) as the sole Fe and S sources. Cell size was determined for each condition using transmission electron microscopy (TEM) (a). Fe content per cell unit volume (assuming coccoid morphology based on TEM measurements) was determined by atomic absorption spectroscopy (b). Data in panel a are means and standard deviations of measured cell diameters from three fields of view for each condition. Data in panel b are means and standard deviations for four biological replicates. Statistical significance was calculated using Student's two-tailed *t* test; *P* values are in the figure.

675 ± 85.6 nm and 450 ± 25.9 nm in diameter, respectively (Fig. 1a; also, see Fig. S1 in the supplemental material). This nearly 33% decrease in diameter in FeS<sub>2</sub>-grown cells related to Fe(II)/HS<sup>-</sup>-grown cells is substantial and, in bacteria, such as *Escherichia coli* and *Bacillus subtilis*, has been suggested to reflect slower growth kinetics associated with the smaller cells (29–31). More recent studies indicate that cell size is more likely a function of nutrient availability, which is in turn inextricably linked with growth kinetics (reviewed in reference 32). In our previous work with *M. voltae*, we observed similar growth kinetics and yields when cells were cultured with formate as the electron donor and with Fe(II)/HS<sup>-</sup> or FeS<sub>2</sub> as the sole Fe and S source (26). For example, the yields of cells cultivated with Fe(II)/HS<sup>-</sup> or FeS<sub>2</sub> as the sole Fe and S source were 1.21 × 10<sup>13</sup> and 1.39 × 10<sup>13</sup> cells mol<sup>-1</sup> CH<sub>4</sub>, respectively. We performed an experiment to convert cell number to cell dry weight in Fe(II)/HS<sup>-</sup>- or FeS<sub>2</sub>-grown cells that were separated from minerals (as described below) and found that Fe(II)/HS<sup>-</sup>-grown cells achieved a mass of 0.111 ± 0.005 μg (dry weight) per million cells, while FeS<sub>2</sub>-grown cells achieved a mass of 0.094 ± 0.010 μg (dry weight) per million cells. Despite methanogens requiring a larger amount of S than Fe (9), we noted that HS<sup>-</sup> accumulated in the growth medium during growth on FeS<sub>2</sub> (26). This indicated that cells were likely replete with S during growth on FeS<sub>2</sub> but may be limited for another nutrient, such as Fe.

In addition to decreased size, cells that are experiencing nutrient limitation oftentimes acclimate by reducing their dependence on those limiting nutrients to assemble biomolecules (reviewed in reference 33). Perhaps the best example is the human pathogen *Borrelia burgdorferi*, which is responsible for Lyme disease. *B. burgdorferi* overcomes the host defense of limiting the availability of Fe in tissues and fluids by eliminating the use of Fe, with individual *B. burgdorferi* cells estimated to contain <10 Fe atoms cell<sup>-1</sup>, through what has been described as an Fe-sparing response (34). Methanogens apparently acclimate similarly. For example, diazotrophic organisms, including methanogens (35), can switch from using a molybdenum (Mo)-dependent nitrogenase to an alternative Mo-independent nitrogenase when Mo is limiting (36, 37). Likewise, the genome of *Methanosarcina acetivorans* has two different gene clusters that encode Mo and tungsten (W)-dependent forms of formylmethanofuran dehydrogenase (Mfr), possibly to allow cellular metabolism to continue when either Mo or W is limiting (38). Finally, methanogens have been shown to acclimate to nickel (Ni) limited conditions by replacing their F<sub>420</sub>-reducing [NiFe] hydrogenase with Ni-independent [Fe] hydrogenase and an F<sub>420</sub>-dependent methylenetetrahydromethanopterin dehydrogenase (5, 39, 40). These precedents prompted experiments to examine Fe usage in *M. voltae* cells.

**Cell iron content.** Based on the above observations, we hypothesized that *M. voltae* cells, when grown with FeS<sub>2</sub>, are Fe limited and would minimize the amount of Fe used when grown on FeS<sub>2</sub>. To examine this hypothesis, we compared the Fe content in *M. voltae* cells provided with Fe(II)/HS<sup>-</sup> or FeS<sub>2</sub> as their sole source of Fe and S. Prior to this analysis, we first developed and validated a technique to separate cells from minerals, so that the latter would not confound measurements of per-cell Fe content. Briefly, cells grown with Fe(II)/HS<sup>-</sup> were harvested at mid-log phase and were enumerated via light microscopy. Roughly  $2.3 \times 10^{10}$  cells were then incubated anaerobically for 60 min in fresh anoxic base salts medium or fresh anoxic base salts medium containing 2 mM synthetic nanoparticulate FeS<sub>2</sub>. Cells were then harvested and subjected to cell separation, washing, and quantification, as detailed in Materials and Methods. Following separation, the total number of cells recovered was similar among treatments ( $4.12 \times 10^9$  and  $3.81 \times 10^9$  cells for unamended and FeS<sub>2</sub>-amended conditions, respectively). A separate aliquot of cells was subjected to digestion with 10% nitric acid, and the lysate was subjected to an analysis of the total Fe content per cell using AA spectroscopy. The amount of Fe per cell was not significantly different between conditions (average of 8 and 11 amol Fe per cell for unamended and FeS<sub>2</sub> conditions, respectively) (Fig. S2). Further, we did not detect FeS<sub>2</sub> nanoparticles associated with cells during counting via light microscopy following separation, nor did we detect paramagnetic FeS<sub>2</sub> signals in whole-cell EPR analyses (discussed below). Together, this indicates that our separation protocol is likely sufficient to remove residual FeS<sub>2</sub>, thereby mitigating the confounding effects that this would have on per-cell Fe analyses.

Following separation of four batches of Fe(II)/HS<sup>-</sup> or FeS<sub>2</sub>-grown cells from mineral and following biomass digestion with 10% nitric acid, the amount of Fe per cell was determined via AA. While the amount of Fe was not significantly different in cultures grown with Fe(II)/HS<sup>-</sup> or FeS<sub>2</sub> on a per-cell basis, when normalized to per unit cell volume, cells cultivated with FeS<sub>2</sub> contained significantly more ( $P=0.03$ ) Fe than those cultivated with Fe(II)/HS<sup>-</sup> (Fig. 1b; Table S1). Specifically, there was a 193% increase in the amount of Fe recovered per unit cell volume in FeS<sub>2</sub>-grown cells compared to those grown with Fe(II)/HS<sup>-</sup>. This was a surprising finding, considering that FeS<sub>2</sub>-grown cells are substantially smaller (which may indicate nutrient limitation) and Fe and S are in excess for both growth conditions. However, the stoichiometries of these elements are different between conditions, with the FeS<sub>2</sub> condition having an Fe:S stoichiometry (1:2) that would seem to favor S limitation while the Fe(II)/HS<sup>-</sup> has an Fe:S stoichiometry (1:80) that could be expected to lead to Fe limitation. These unexpected observations prompted additional analyses to identify potential differences in the trafficking, deployment, and storage of Fe in FeS<sub>2</sub>- versus Fe(II)/HS<sup>-</sup>-grown cells.

**Whole-cell EPR.** To provide insight into possible destinations for Fe in Fe(II)/HS<sup>-</sup>- versus FeS<sub>2</sub>-grown cells, we applied EPR spectroscopy to whole-cell samples. These samples were a larger subsample of the same cells that were treated to remove residual FeS<sub>2</sub> nanoparticles, if present, and used to quantify Fe content via AA as described above (Table S1). We collected EPR spectra from the base salts medium as a control and observed limited background signals near a  $g$  factor value of  $\sim 2$  (Fig. S3). We also collected EPR spectra from synthetic FeS<sub>2</sub> and FeS<sub>mack</sub> and observed unique, broad paramagnetic signals that are absent in the whole-cell EPR spectra, suggesting that the whole-cell–mineral separation techniques were effective in removing mineral (Fig. S4). Low-temperature EPR spectral analysis of Fe(II)/HS<sup>-</sup> and FeS<sub>2</sub>-grown *M. voltae* whole cells revealed highly similar, axial shaped signals with  $g$  values spanning the 1.94-to-2.05 region in both sample treatments (Fig. 2a). EPR spin quantitation of these signals revealed that Fe(II)/HS<sup>-</sup>-grown cell samples averaged  $16.0 \pm 1.1 \mu\text{M spin}$  ( $\sim 0.5\%$  total Fe) and FeS<sub>2</sub>-grown cell samples averaged  $20.3 \pm 10.4 \mu\text{M spin}$  ( $\sim 1.3\%$  total Fe). EPR spectra were collected at a range of temperatures to provide further insights into the origins of these signals. Substantial signal intensity loss was observed for the 1.94–2.05 features as the temperature was increased from 12 to 30 K, and these signals were not observed at 50 K (Fig. 2b; Fig. S2). The axial line shape, the  $g$  values, and the strongly temperature-dependent relaxation properties support the assignment of these features primarily to biological [4Fe-4S]<sup>+</sup> cluster species (4, 41–45).

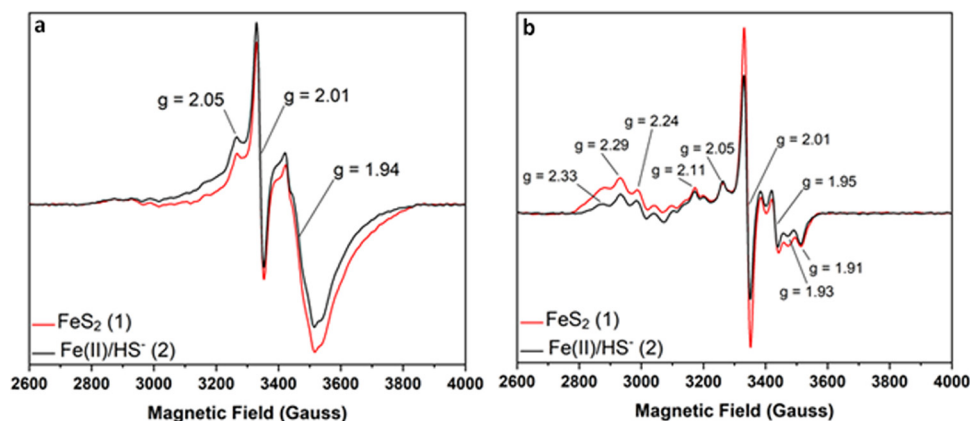


**FIG 2** Electron paramagnetic resonance (EPR) spectra for *Methanococcus voltae* whole cells grown with pyrite or ferrous iron and sulfide. Cells were grown with formate and either synthetic pyrite nanoparticles ( $\text{FeS}_2$ ) or ferrous iron and sulfide  $[\text{Fe(II)/HS}^-]$  and then separated from mineral species as described in the text. Data were collected at X-band at both 12 K (a) and 50 K (b) at 5 mW microwave power. The spectra shown in this figure have been baseline and cavity corrected in order to directly overlay the spectroscopic [Fe-S] cluster signals between the different growth conditions. Samples shown are designated in Table S1.

These samples additionally show evidence in the low-field region for integer spin species, perhaps a rubredoxin-like Fe(II), with  $g$  values of  $\sim 10$ . Signals having the characteristic line shape,  $g$  values ( $g = \sim 4$  to  $6$ ), and temperature relaxation properties of  $S = 3/2$   $[4\text{Fe-4S}]^+$  clusters are also observed (Fig. S5) (44, 46–49). EPR spectra of  $\text{Fe(II)/HS}^-$  and  $\text{FeS}_2$ -grown *M. voltae* whole-cell samples at higher temperatures (50 and 75 K) revealed several overlapping signals in both sample treatments, with  $g$  values spanning the 1.91–2.33 region (Fig. 2b). Given the  $g$  values and temperature dependence, these signals may arise from species such as the  $F_{430}$  nickel porphyrinoid of methyl CoM reductase, the noncubane  $[4\text{Fe-4S}]$  clusters in heterodisulfide reductase, and the molybdenum guanine dinucleotide cofactor of Mfr (50–55). The rich complexity of the signals likely also reflects several additional metallocofactor species, as well as biological  $[2\text{Fe-2S}]^+$  clusters (41, 43, 56, 57). The observation of rubredoxin-like and  $[4\text{Fe-4S}]^+$  cluster species in these samples is not unexpected, given the abundance of proteins with [Fe-S] motifs in methanogens (8, 10) and their detection in proteomics data from these cells (described below). Collectively, these data show that cells growing with  $\text{Fe(II)/HS}^-$  or  $\text{FeS}_2$  synthesize a similar array of proteins that have similar abundances and compositions of EPR-detectable [Fe-S] clusters.

EPR spectra of  $\text{FeS}_2$ -grown *M. voltae* whole-cell samples collected over a wide magnetic field revealed additional broad signals of variable intensity spanning  $\sim 3,000$  G and centered near a  $g$  value of 2.2 (Fig. 3a). This broad signal undergoes gradual intensification as the temperature is raised from 8 K to 100 K, before relaxing substantially when temperature is further increased to 150 K (Fig. 4a). The breadth of the EPR signal and its temperature dependence are largely consistent with those described for the Fe-S storage protein A (IssA) from the archaeon *Pyrococcus furiosus* (58). IssA stores Fe and S as linear  $(\text{FeS}_2^-)_n$  thioferrate polymer nanostructures, and EPR spectroscopic characterization of purified IssA-thioferrate complexes reveals signal intensification up to 250 K, behavior that is consistent with synthetic potassium thioferrate species (59). The highly similar broad EPR signal observed here for  $\text{FeS}_2$ -grown *M. voltae* whole cells (Fig. 4a), together with the different temperature dependence reported herein, could indicate that these cells accumulate a different type of Fe-S nanostructure, similar to but distinct from the thioferrate structures assembled in *P. furiosus* with IssA. Further, the broad signal we observe accounts for appreciable spin, estimated at between  $\sim 100$  and  $\sim 610 \mu\text{M}$  paramagnetic species (10 to 23% total Fe) based on double integration of the EPR signal. Together with the evidence that  $\text{FeS}_2$ -grown cells contain nearly double the Fe per unit volume relative to cells grown on  $\text{Fe(II)}$  and  $\text{HS}^-$ , the broad EPR signal is consistent with *M. voltae* accumulating and storing Fe, perhaps as a type of

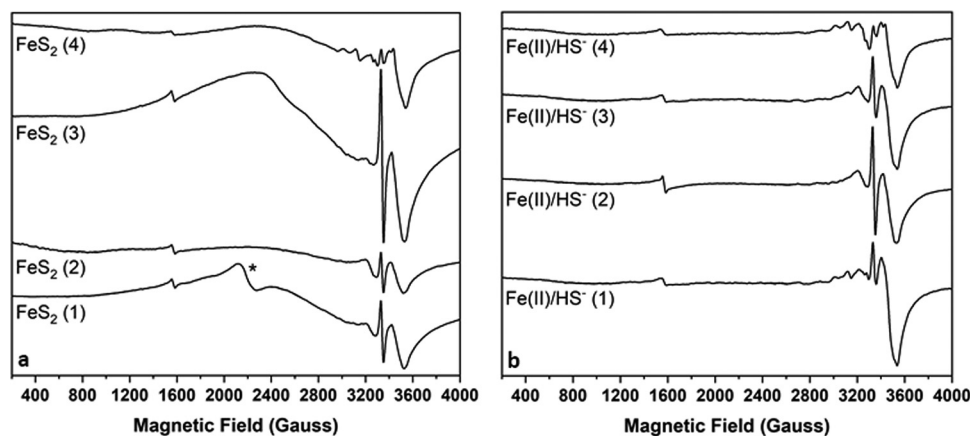


**FIG 3** Broad-field EPR spectra for *Methanococcus voltae* whole-cell samples grown with either pyrite or ferrous iron and sulfide. Cells were grown with formate and either synthetic pyrite nanoparticles ( $\text{FeS}_2$ ) (a) or ferrous iron and sulfide [ $\text{Fe(II)/HS}^-$ ] (b) and then separated from mineral species as described in the text. Data were collected at X-band, with 5 mW microwave power and a temperature of 8 K. The spectra shown in this figure have not been baseline or cavity corrected. The cavity contribution to the signals near a  $g$  value of  $\sim 2.0$  is negligible (see the supplemental material). The asterisk denotes a paramagnetic species ( $g, \sim 3.0$ ) of unknown origin. Samples shown are designated in Table S1.

Fe-S nanostructure. Importantly,  $\text{Fe(II)/HS}^-$ -grown *M. voltae* cells exhibit either very low or undetectable amounts of this broad signal (Fig. 3b and 4b; Fig. S6), indicating that the putative thioferrate-like nanoparticles do not accumulate to nearly the same extent as they do in  $\text{FeS}_2$ -grown *M. voltae* cells (Fig. 3).

**Differential proteomics analyses.** To further characterize differences in the core energy metabolism and potential protein destinations for Fe in  $\text{Fe(II)/HS}^-$ - or  $\text{FeS}_2$ -grown *M. voltae* cells, a differential proteomics approach was undertaken. We first conducted an experiment to confirm that the presence of  $\text{FeS}_2$  does not influence the recovery of protein following extraction, using a design similar to that used for whole-cell AA/EPR analysis. Briefly,  $\text{Fe(II)/HS}^-$ -grown cells were harvested, and the pelleted biomass was split for incubation with sterile fresh medium with or without 2 mM  $\text{FeS}_2$  added. The samples were incubated on ice for 30 min, the cells were reharvested, and the resultant cell pellets were subjected to protein extraction. SDS-PAGE analysis

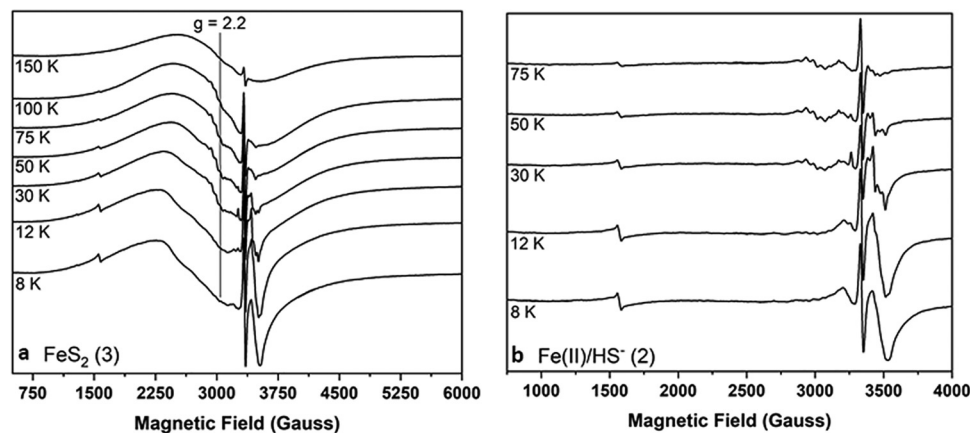


**FIG 4** Variable-temperature, continuous-wave (CW) X-band electron paramagnetic resonance (EPR) for *Methanococcus voltae* whole cells grown with formate and either synthetic pyrite ( $\text{FeS}_2$ ) nanoparticles (a) or ferrous iron [ $\text{Fe(II)}$ ] and sulfide ( $\text{HS}^-$ ) (b). Whole cells were characterized at 5 mW microwave power as a function of increasing temperature. Importantly, the spectra shown in this figure have not been baseline or cavity corrected. The cavity contribution to the signals near a  $g$  value of  $\sim 2.0$  is negligible (see the supplemental material), and we endeavored to preserve the baseline signatures in all data sets due to the variable intensity of thioferrate-like signals. Samples shown are designated in Table S1.

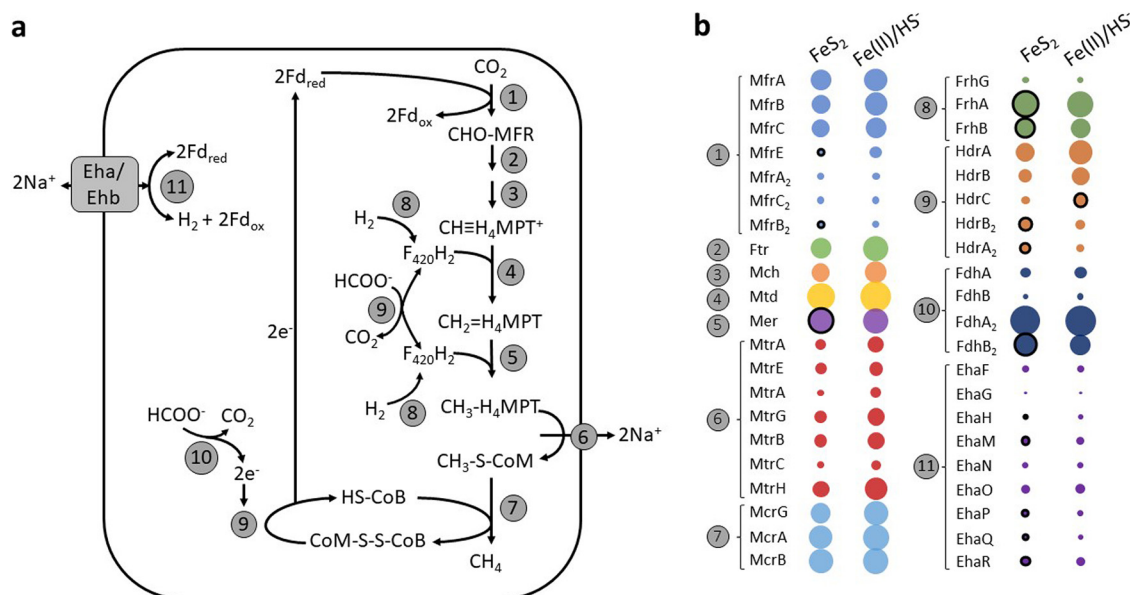


**FIG 5** Abundances of core methanogenesis pathway proteins in *Methanococcus voltae* cells grown with different iron (Fe) and sulfur (S) sources. Proteins were extracted from log-phase *M. voltae* cells provided with formate and synthetic pyrite nanoparticles (FeS<sub>2</sub>) or ferrous iron [Fe(II)] and sulfide (HS<sup>-</sup>). A model for methanogenesis supported by formate, including replenishment of intermediates through membrane-bound and ion-translocating [NiFe] hydrogenase (Eha/Ehb), is shown in panel a. The relative abundances of key methanogenesis proteins for reactions identified in panel a are presented for FeS<sub>2</sub> and Fe(II)/HS<sup>-</sup> conditions in panel b. Bubble sizes for each protein in panel b represent the mean of the normalized spectral intensity of three biological replicates per condition. Bubbles are colored based on function, with black outlines indicating proteins that are significantly ( $P < 0.05$ ;  $\log_2 \text{FC} > 1$ ) up-expressed under one condition relative to the other. Enzyme names and abbreviations for each step in methanogenesis are as follows: 1, formylmethanofuran dehydrogenase (Mfr); 2, formylmethanofuran:tetrahydromethanopterin (H<sub>4</sub>MPT) formyltransferase (Ftr); 3, methenyltetrahydromethanopterin cyclohydrolase (Mch); 4, F<sub>420</sub>H<sub>2</sub>-dependent methylenetetrahydromethanopterin dehydrogenase (Mtd); 5, coenzyme F<sub>420</sub>-dependent N<sup>5</sup>,N<sup>10</sup>-methylene tetrahydromethanopterin reductase (Mer); 6, methyl-H<sub>4</sub>MPT-coenzyme M methyltransferase (Mtr); 7, methyl coenzyme M reductase (Mcr); 8, coenzyme F<sub>420</sub>-reducing [NiFe] hydrogenase (Frh); 9, heterodisulfide reductase (Hdr); 10, formate dehydrogenase (Fdh); 11, energy-converting [NiFe] hydrogenase (Eha/Ehb).

showed no noticeable differences in protein banding patterns between the two conditions (Fig. S7), and protein quantification via NanoDrop indicated similar protein recoveries (averages of 2.95 and 2.90 mg protein ml<sup>-1</sup> for cells incubated with FeS<sub>2</sub> versus those not incubated with FeS<sub>2</sub>, respectively). These observations indicate that the presence of FeS<sub>2</sub> does not substantively interfere with the composition or abundance of proteins following extraction.

*M. voltae* was grown with synthetic nanoparticulate FeS<sub>2</sub> or Fe(II)/HS<sup>-</sup>, and cell CH<sub>4</sub> concentrations were determined before proteins were extracted from cells in mid-log phase (Table S2). Differential proteomics analyses identified broad differences in the global proteome of *M. voltae* between these conditions (Fig. S8). We then narrowed our analyses to the abundance of proteins that are involved in the core pathway of methanogenesis (1, 60) to determine if growth on FeS<sub>2</sub> had an influence on the overall energetic state of cells. Broadly, we did not detect substantive differences in many of the core proteins for methanogenesis between cells growing with Fe(II)/HS<sup>-</sup> and those growing with FeS<sub>2</sub> (Fig. 5; Data Set S1). However, heterodisulfide reductase subunits HdrB<sub>2</sub> and HdrA<sub>2</sub>, the F<sub>420</sub>-reducing hydrogenase subunits FrhA and FrhB, and one subunit of a second copy of formylmethanofuran dehydrogenase, MfrB<sub>2</sub>, were slightly up-expressed under the FeS<sub>2</sub> growth condition compared to the Fe(II)/HS<sup>-</sup> growth condition. Conversely, MfrE and HdrC were slightly down-expressed in cells grown on FeS<sub>2</sub> relative to those grown on Fe(II)/HS<sup>-</sup>. While these subtle differences represent changes in expression of several subunits, no complete enzyme complex involved in methanogenesis displayed differential expression. Thus, the energy metabolism of *M. voltae* appears to be similar when cells are grown with Fe(II)/HS<sup>-</sup> and FeS<sub>2</sub>.

Using informatics approaches (61), we next identified proteins with putative [Fe-S] cluster binding domains, as these proteins could be involved in assimilating and/or trafficking the putative reductive dissolution product of FeS<sub>2</sub> reduction, FeS<sub>aq</sub>. A total of 101 proteins

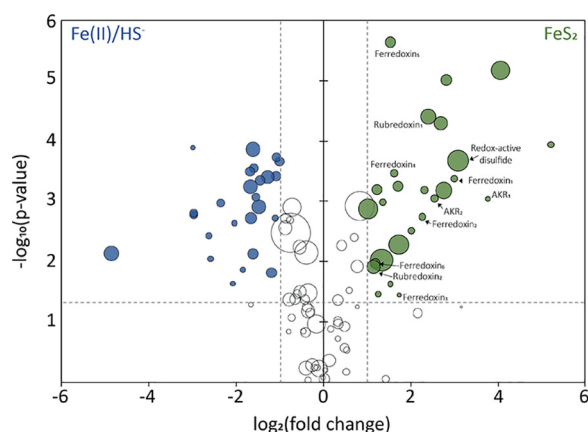


**FIG 6** Differential expression of proteins predicted to bind iron-sulfur ([Fe-S]) clusters in *Methanococcus voltae*. *M. voltae* was grown to mid-log phase with formate and synthetic pyrite (FeS<sub>2</sub>) nanoparticles or ferrous iron [Fe(II)] and sulfide (HS<sup>-</sup>) as sole iron and sulfur sources. The data presented are limited to proteins that are predicted to bind [Fe-S] clusters, as determined with MetalPredator (61), in the proteomics data set. Along the x axis, a positive log<sub>2</sub> FC is associated with up-expression of proteins in FeS<sub>2</sub>-grown cells, whereas a negative log<sub>2</sub> FC is associated with up-expression of proteins in Fe(II)/HS<sup>-</sup>-grown cells. The bubble size for each protein represents the mean normalized spectral intensity of three biological replicates for FeS<sub>2</sub>-grown cells (positive log<sub>2</sub> FC) or for Fe(II)/HS<sup>-</sup>-grown cells (negative log<sub>2</sub> FC). The significance of differential expression for each protein, calculated as  $-\log_{10}(P)$ , is plotted along the y axis, with increasing values indicating higher statistical significance. Colored bubbles indicate proteins with significant ( $P < 0.05$ ) differential expression with a log<sub>2</sub> FC of at least 1. Dashed lines show cutoff values for significance and log<sub>2</sub> FC.

with [Fe-S]-binding motifs were predicted in the *M. voltae* proteome. Of these, 52 were significantly differentially expressed between FeS<sub>2</sub>-grown and HS<sup>-</sup>/Fe(II)-grown cells ( $P < 0.05$ ; log<sub>2</sub> fold change [FC] > 1), half of which were up-expressed on FeS<sub>2</sub> (Fig. 6; Data Set S1). Interestingly, a putative redox-active disulfide protein (*Mvol\_1251*), the 19th most highly detected protein in the entire FeS<sub>2</sub> proteome, was significantly up-expressed in the FeS<sub>2</sub> growth condition (FC, 8.45;  $P < 0.01$ ). This protein is uncharacterized but shows homology to putative archaeal thioredoxins. Further, six of the 17 putative [4Fe-4S] ferredoxin binding domain proteins encoded in the *M. voltae* genome were significantly up-expressed in the FeS<sub>2</sub>-grown cells, while only two were up-expressed in Fe(II)/HS<sup>-</sup>-grown cells; the remaining nine were similarly expressed between the two growth conditions. One of these proteins (*Mvol\_0876*) is homologous to formylmethanofuran dehydrogenase, subunit G (FwdG) and is found in a gene cluster with other Fwd-encoding genes. In addition, two of these proteins (*Mvol\_1602* and *Mvol\_1603*) are homologous to subunits of the membrane-bound hydrogenase (Eha), EhaP, and EhaQ, respectively. Inferred functions of the other three up-expressed putative ferredoxin-binding proteins (*Mvol\_0606*, *Mvol\_1449*, and *Mvol\_0711*) could not be established based on homology to characterized proteins or on functionalities of proteins encoded by adjacent genes. The genome of *M. voltae* encodes two rubredoxin proteins, both of which were significantly up-expressed on FeS<sub>2</sub>, supporting our observation of features consistent with rubredoxin in EPR spectra of FeS<sub>2</sub>-grown cells (Fig. 6; Fig. S5). Two aldo-/ketoreductases are encoded in the *M. voltae* genome, and both were significantly up-expressed on FeS<sub>2</sub> as well. The aldo-/ketoreductases are currently being evaluated for their potential role(s) in supplying reducing equivalents for the reduction of FeS<sub>2</sub>.

We next examined the abundance of proteins that might be involved in Fe transport in *M. voltae* using informatics approaches. In bacteria, the Feo system functions to transport Fe(II) into the cell (62, 63). The transmembrane protein, FeoB, is generally accompanied by a soluble component, FeoA, that has a regulatory function (63). NTP-driven, FeoAB-mediated transport of Fe(II) has been suggested to be the primary mechanism of incorporating Fe in methanogens based on informatics data (64). The proteome of *M. voltae* contains two copies of FeoA (*Mvol\_0977* and *Mvol\_0619*), both of which were significantly up-expressed in cells grown with FeS<sub>2</sub> relative to those grown with Fe(II)/HS<sup>-</sup>. Adjacent to the more highly expressed FeoA gene is a gene encoding FeoB (*Mvol\_0975*), which was also significantly up-expressed

when cells were grown on  $\text{FeS}_2$  compared to  $\text{Fe(II)/HS}^-$  (Data Set S1). Similarly, a homolog of DtxR (*Mvol\_0620*), a negative transcriptional regulator involved in maintaining transition metal homeostasis in *Bacteria* and some *Archaea* (65–67), was up-expressed in  $\text{FeS}_2$ - versus  $\text{Fe(II)/HS}^-$ -grown cells. When  $\text{Fe(II)}$  is limiting and is unavailable, DtxR is inactive. Conversely, when DtxR binds available  $\text{Fe(II)}$ , it suppresses genes involved in Fe uptake and transport, such as FeoAB, to maintain cytoplasmic Fe homeostasis (65–67). Increased expression of DtxR and FeoAB could imply that the cells incorrectly sense  $\text{Fe(II)}$  limitation when grown with  $\text{FeS}_2$  compared to those grown with  $\text{Fe(II)/HS}^-$ . This is potentially consistent with the smaller size of cells grown with  $\text{FeS}_2$  compared to those on  $\text{Fe(II)/HS}^-$  (Fig. 1a), possibly attributable to perceived nutrient (i.e., Fe) limitation. However,  $\text{FeS}_2$ -grown cells accumulate 193% more Fe per unit cell volume than  $\text{Fe(II)/HS}^-$ -grown cells (Fig. 1b), and this extra Fe is possibly stored as a thioferate-like phase, based on EPR data (Fig. 3 and 4). Given that cells were growing at the same rate and were in the same stage of growth when they were harvested for analyses, as shown in growth curves reported in a recently published article (26), these differences are attributed to the different Fe and S sources used to cultivate cells.

The apparent contradiction between sensed iron limitation and iron hyperaccumulation (in an *IssA*-type, mineralized context and/or an abundance of [Fe-S]-binding proteins) may be less a consequence of the intracellular availability of Fe than of S, under the growth conditions used, considering that cells need more S than they do Fe (9). We hypothesize that to simultaneously meet Fe and S demands, cells passively assimilate uncharged  $\text{FeS}_{\text{aq}}$  or  $\text{FeSH}^+$ , facilitated via an unknown transporter.  $\text{FeS}_{\text{aq}}$  could be generated either through dissolution of  $\text{FeS}_{\text{mack}}$  or  $\text{Fe}_{1-x}\text{S}_{\text{pyr}}$  that has reductively precipitated onto the surface of  $\text{FeS}_2$  (27), or from spontaneous association of  $\text{Fe(II)}$  and  $\text{HS}^-$  to form  $\text{FeS}_{\text{aq}}$  when  $\text{HS}^-$  concentrations exceed  $>1\ \mu\text{M}$  (15), as in the experiments outlined herein. Passive assimilation would occur along the concentration gradients for Fe and S, which would be expected to favor uptake of FeS into the cell. Further metabolism of the Fe and S once inside the cell may favor immediate deposition into storage formats like *IssA*-thioferate when intracellular S availability is low relative to Fe, particularly if intracellular trafficking and usage of  $\text{Fe(II)}$  occur in conjunction with  $\text{HS}^-$  or thiolate ligands. Alternatively, resorption of Fe out of a mineralized storage phase may obligately require the participation of S species. Further investigations into the role of the DtxR/FeoAB system(s) in Fe transport and regulation and possible coregulation of S metabolic pathways are needed to evaluate these hypotheses.

The observation of similar levels of expression of proteins involved in core methanogenesis pathways and similar (note exceptions above) levels of expression of putative [Fe-S] binding proteins in the proteomes of *M. voltae* grown with  $\text{Fe(II)/HS}^-$  versus those grown with  $\text{FeS}_2$  implies that the pathways of trafficking Fe/S in these cells are largely similar. Little is known of how Fe and S are trafficked in methanogens, although informatics analyses reveal that the only known [Fe-S] cluster biosynthesis pathway in these cells is the sulfur pathway (SUF) (8, 68). Originally described in *Escherichia coli* (69), the full SUF system is composed of the genes *sufABCDSE* (70, 71). However, the genome of *M. voltae* encodes homologs of only a scaffold protein, *SufB* (*Mvol\_0653*), and the ATPase *SufC* (*Mvol\_0654*) and lacks homologs of cysteine desulfurase (*SufS*) (8), which, in *E. coli* and other cells (72), donates S from cysteine to *SufBC* for [Fe-S] cluster biosynthesis. This lack of a *SufS* homolog is consistent with the inability of *M. voltae* to use cysteine as a S source for growth (73).

In methanogens, cysteine is synthesized from  $\text{HS}^-$  (9) via the tRNA-dependent SepRS/SepCysS pathway (74). First, tRNACys is aminoacylated with *O*-phosphoserine (Sep) via the activity of *O*-phosphoserine-tRNA synthetase (SepRS). Next, Sep-tRNACys is converted to CystRNACys by Sep-tRNA:Cys-tRNA synthase (SepCysS). *M. voltae* encodes homologs of both enzymes (*Mvol\_0433* and *Mvol\_0651*, respectively). To gauge if *M. voltae* alters how it processes/traffics Fe and S for [Fe-S] cluster and cysteine biosynthesis using the SUF and SepRS/SepCysS pathways, respectively, when grown on  $\text{FeS}_2$  versus  $\text{Fe(II)/HS}^-$ , we compared the profiles of the peptides from each pathway. No significant differences in expression of *SufBC* were detected in cells grown on either source of Fe and S. While we detected over 75% of proteins from the predicted proteome of *M. voltae*, we did not capture peptides that match SepRS. However, SepCysS was detected under both

growth conditions at similar levels. Thus, *M. voltae* does not appear to alter the expression of either the *SUF* or *SepRS/SepCysS* pathways in response to growth on  $\text{FeS}_2$ .

We next examined the genome of *M. voltae* for proteins with homology to the *IssA* homolog identified in *P. furiosus* that coordinates thioferrate as a mechanism to store Fe and S. Specifically, we examined the genome for protein homologs that encode the N-terminal 1 to 109 residues (IPR003731 domain) of *P. furiosus* *IssA*, since this domain has been overexpressed, purified, and biochemically shown to be capable of binding 25 equivalents of Fe per monomer (58). Two proteins encoded in the *M. voltae* genome (*Mvol\_0689* and *Mvol\_0693*) exhibited homology (25% and 27% sequence identities) to the N-terminal domain of *P. furiosus* *IssA*, and both were upregulated under the  $\text{FeS}_2$  growth condition (Data Set S1). The up-expression of *Mvol\_0689* and *Mvol\_0693* gene products in  $\text{FeS}_2$ - relative to  $\text{Fe(II)/HS}^-$ -grown cells is possibly consistent with a role in Fe/S metabolism, since this is the only variable that differs in this treatment. As mentioned above, it is possible that one or both homologs function to store or sequester thioferrate-like nanoparticles during growth with  $\text{FeS}_2$ . Alternatively, given the unique temperature relaxation profile for the broad signal in *M. voltae* cells tentatively assigned to thioferrate-like particles (Fig. 4), it is possible that these gene products or other unknown proteins act to stabilize different forms of Fe/S-based nanoparticles. To further assess this possibility, we examined TEM images of *M. voltae* cells grown with  $\text{Fe(II)/HS}^-$  or  $\text{FeS}_2$ . A greater abundance of electron-dense regions was observed in  $\text{FeS}_2$ -grown cells that could be attributable to Fe-containing nanoparticles in the cytoplasm of the cells. However, similar electron dense regions were also observed in  $\text{Fe(II)/HS}^-$  grown cells, albeit to a lesser extent (Fig. S1). Additional work will be necessary to determine whether *IssA* homologs in *M. voltae* can coordinate Fe/S nanoparticles, to determine the form of Fe/S that is stored/sequestered in these nanoparticles, and to determine whether Fe/S storage/sequestration as nanoparticles represents a mechanism for cells to maintain Fe homeostasis.

**Conclusions.** *M. voltae* exhibits clear phenotypic differences in response to growth with  $\text{Fe(II)/HS}^-$  and with  $\text{FeS}_2$ . Distinct differences in cell morphology were observed between growth conditions, most notably the significantly reduced size of cells growing with  $\text{FeS}_2$  compared to those grown with  $\text{Fe(II)/HS}^-$ . While the cells are smaller, it is not necessarily due to an effect of Fe limitation, as the cells from the  $\text{FeS}_2$  growth conditions were found to have more Fe on a per-cell volumetric basis than those grown with  $\text{Fe(II)/HS}^-$ . Differential proteomics analyses suggest little if any difference in the energetic state of cells grown with  $\text{FeS}_2$  versus  $\text{Fe(II)/HS}^-$ , as indicated by similar abundances of proteins involved in the core energy metabolism pathways of these cells. Differential proteomics analyses and whole-cell EPR identified some difference in the expression and deployment of [Fe-S] clusters among the proteomes of  $\text{FeS}_2$ - versus  $\text{Fe(II)/HS}^-$ -grown cells, including in small putative ferredoxin and rubredoxin domain proteins, as well as several oxidoreductases (e.g., aldo-/ketoreductases and redox-active disulfide protein) that are currently being evaluated for their potential roles in supplying reducing equivalents for the reduction of  $\text{FeS}_2$ .

A broad EPR signal observed in  $\text{FeS}_2$ -grown cells but not in  $\text{Fe(II)/HS}^-$ -grown cells, combined with proteomics data indicating up-expression of two homologs of *IssA* in *M. voltae* and the observation of electron-dense regions in cells growing with  $\text{FeS}_2$ , suggests that *M. voltae* may store Fe/S as thioferrate-like nanoparticles, similar to what has been described for *P. furiosus* (58). However, the temperature dependence of the broad EPR signal observed for *M. voltae* cells grown with  $\text{FeS}_2$  suggest that the Fe/S phase is likely distinct from the thioferrate phase previously detected in *P. furiosus* cells. Nonetheless, these combined observations indicate that *M. voltae* cells accumulate Fe when grown on  $\text{FeS}_2$  relative to  $\text{Fe(II)/HS}^-$ . Paradoxically, differential proteomics analyses revealed that two homologs of *FeoA* and a single homolog of *FeoB* putatively involved in transport of Fe(II) and a transcriptional regulator (*DtxR*) putatively involved in sensing Fe(II) and regulating Fe homeostasis were upregulated in  $\text{FeS}_2$ - versus  $\text{Fe(II)/HS}^-$ -grown cells. This indicates that cells incorrectly sense Fe limitation when grown

with FeS<sub>2</sub>. These observations could suggest that the intracellular metabolism of the stored Fe depends on the availability of excess S species that either intercept the Fe prior to deposition into storage or are necessary for its retrieval from the stored phase.

We put forward a model for Fe/S acquisition, deployment, and storage/sequestration aimed at reconciling observations that collectively point to cells apparently sensing and responding to Fe limitation while at the same time pointing to enhanced Fe storage/sequestration in FeS<sub>2</sub>-grown cells, relative to Fe(II)/HS<sup>-</sup>-grown cells. Following cell-mediated reduction of FeS<sub>2</sub>, FeS<sub>mack</sub> or Fe<sub>1-x</sub>S<sub>pyr</sub> precipitates on the surface of FeS<sub>2</sub> (27), and dissolution of FeS<sub>mack</sub> or Fe<sub>1-x</sub>S<sub>pyr</sub> in the presence of >1 μM sulfide favors FeS<sub>aq</sub> cluster species as the predominant form of Fe(II) in solution (15). Such species could be scavenged and transported into the cell in protein-bound states. Alternatively, one could envision direct transport of FeS<sup>0</sup> or FeSH<sup>+</sup> via as-yet-unidentified transporters. Either situation could lead to excess Fe (and possibly S) in the cell that is stored/sequestered as thioferrate-like nanoparticles, since the Fe and S are assimilated in an ~1:1 ratio and cells require more S than Fe (9). In this model, DtxR, which binds Fe(II) under Fe-replete conditions and downregulates expression of proteins involved in Fe assimilation, such as FeoAB (65–67), would not sense Fe(II), since it is present primarily as FeS<sub>aq</sub> and/or protein-bound FeS species. The lack of Fe(II) binding to DtxR would lead to accumulation of Fe in the cell that is stored or sequestered by IssA-like homologs as thioferrate-like species, as mechanism to limit Fe toxicity. This model provides a framework for the rational design of targeted physiological, biochemical, and genetic experiments aimed at further characterizing Fe acquisition and homeostasis in *M. voltae*, with possible application to other methanogens.

## MATERIALS AND METHODS

**Preparation of synthetic nanoparticulate pyrite.** All chemicals used in mineral synthesis were American Chemical Society grade or higher. All glassware was first washed in 10% nitric acid and rinsed three times with 18.2-Ω Milli-Q water (MQ H<sub>2</sub>O). Pyrite (FeS<sub>2</sub>) was synthesized according to methods outlined by Berner (16). Briefly, within an anaerobic chamber (Coy Labs, Grass Lake, MI), 14.4 g Na<sub>2</sub>S · 9H<sub>2</sub>O and 16.7 g FeSO<sub>4</sub> · 7H<sub>2</sub>O were separately dissolved in 50 ml of anoxic MQ H<sub>2</sub>O. These two solutions were then combined in a 500-ml bottle and stirred vigorously for 15 min, at which point 2.1 g of elemental sulfur (S<sup>0</sup>) was added. The bottle was then sealed with a butyl rubber stopper, removed from the chamber, and bubbled with N<sub>2</sub> passed over heated (200°C) and H<sub>2</sub>-reduced copper shavings for 45 min. Following purging, the solution was incubated anoxically for 4 days at 65°C and then for another 4 days at 85°C. After incubation, the FeS<sub>2</sub> was washed aerobically in sealed centrifuge tubes (via centrifugation [1,000 × g, 10 min, 4°C] and decanting) in the following series to remove unreacted HS<sup>-</sup>, Fe(II), FeS, and S<sup>0</sup>: four rinses with 1 N HCl, one rinse with boiling 6 N HCl, two rinses with MQ H<sub>2</sub>O, and three rinses with >99.5% acetone. The FeS<sub>2</sub> was then transferred to an anaerobic chamber and further washed three times with sterile MQ H<sub>2</sub>O. After washing, the FeS<sub>2</sub> was pelleted via centrifugation (1,000 × g, 10 min, 4°C) and transferred back into an anaerobic chamber; the aqueous phase was decanted, and the pellet was resuspended in sterile, anoxic MQ H<sub>2</sub>O in a butyl rubber-stoppered sterile serum bottle. Finally, the headspace of the bottle was purged with 0.2-μm-filtered ultra-high-purity N<sub>2</sub> gas. The percentage (wt/vol) of the slurry was determined by drying 1 ml of slurry in triplicate under N<sub>2</sub> and weighing the dried product. FeS<sub>mack</sub> used here in EPR experiments, was synthesized as we described previously (26).

**Strains and cultivation medium.** *Methanococcus voltae* strain A3 was obtained from the American Type Culture Collection (ATCC-BAA-1334). *M. voltae* was grown in Fe- and S-free basal medium that contained the following (in grams per liter): NaCl, 21.98; MgCl<sub>2</sub> · 6H<sub>2</sub>O, 5.10; NaHCO<sub>3</sub>, 5.00; NH<sub>4</sub>Cl, 0.50; K<sub>2</sub>HPO<sub>4</sub>, 0.14; KCl, 0.33; and CaCl<sub>2</sub> · 2H<sub>2</sub>O, 0.10 (Table S3). The basal medium was amended with 0.01 g liter<sup>-1</sup> Fe(NH<sub>4</sub>)<sub>2</sub>(SO<sub>4</sub>)<sub>2</sub> · 6H<sub>2</sub>O and 0.48 g liter<sup>-1</sup> Na<sub>2</sub>S · 9H<sub>2</sub>O for Fe(II)/HS<sup>-</sup>-grown cells after autoclaving. Sulfide was added from an anoxic, sterile stock solution 30 min prior to inoculation. For FeS<sub>2</sub>-grown cells, basal medium was amended with FeS<sub>2</sub> to a final concentration of 2 mM Fe prior to inoculation. Basal medium was amended (each 1% [vol/vol]) with trace element, vitamin, formate, and organic solutions prior to inoculation. The trace element solution used was based on the work of Whitman et al. (73) and was amended to omit Fe and replace sulfate salts with chloride salts at the same molar concentrations. The trace element solution contained the following (in grams per liter): nitrioloacetic acid, 1.500; MnCl<sub>2</sub> · 4H<sub>2</sub>O, 0.085; CoCl<sub>2</sub> · H<sub>2</sub>O, 0.100; ZnCl<sub>2</sub>, 0.047; CuCl<sub>2</sub> · 2H<sub>2</sub>O, 0.0683; NiCl<sub>2</sub> · 6H<sub>2</sub>O, 0.0683; Na<sub>2</sub>SeO<sub>3</sub>, 0.200; Na<sub>2</sub>MoO<sub>4</sub> · 2H<sub>2</sub>O, 0.100; and Na<sub>2</sub>WO<sub>4</sub> · 2H<sub>2</sub>O, 0.100. The vitamin solution contained (in grams per liter): pyridoxine HCl, 0.01; thiamine HCl, 0.005; riboflavin, 0.005 g; nicotinic acid, 0.005; calcium D(+) pantothenate, 0.005; biotin, 0.002; folic acid, 0.002; and cobalamin, 0.0001. The organic solution consisted of 1 M sodium acetate · 3H<sub>2</sub>O, 75 mM L-leucine HCl, and 75 mM L-isoleucine HCl. The formate solution contained 40% (wt/vol) sodium formate.

All basal medium components, except NaHCO<sub>3</sub>, were dissolved in MQ H<sub>2</sub>O and then boiled for 15 min. After boiling, the medium was sealed with a butyl rubber stopper and sparged with N<sub>2</sub> gas passed over a heated (200°C) and reduced copper column for 1 h per liter of medium. After degassing, the medium was sealed and brought into an anaerobic chamber, and NaHCO<sub>3</sub> was added as specified

above. After addition of these components, the pH of the medium was adjusted to 7.00 using anoxic 2 M HCl or 1 M NaOH. For proteomic experiments, 75 ml of medium was dispensed into 165-ml serum bottles. For AA and EPR experiments, as well as experiments aimed at testing cell-mineral separation techniques, 800 ml of medium was dispensed into 2-liter medium bottles. Once dispensed, bottles were sealed with 20-mm black rubber stoppers and aluminum crimp caps (165-ml serum bottles) or with number 6.5 black rubber stoppers and sealed with screw-cap tops that had been modified by drilling to provide a sampling port to access the stopper (2-liter medium bottles). The headspace of the medium bottles was purged with 80:20 N<sub>2</sub>-CO<sub>2</sub> for 30 min. Two-liter medium bottles were carefully vented with a 22-gauge needle to ~1 atm and stored upside down in individual metal autoclave bins to minimize in-gassing of O<sub>2</sub> from the atmosphere and to ensure the safety of personnel during autoclaving, respectively. The bottles were then autoclaved for 20 min at 123°C.

**Cultivation of *M. voltae*.** Cultures of *M. voltae* were maintained by weekly transfers (10% [vol/vol]) into fresh medium with formate as the methanogenesis substrate and Fe(II) and HS<sup>-</sup> as sole Fe and S sources, respectively. Cells were washed prior to inoculation by pelleting them in sealed 50-ml tubes (Globe Scientific, Mahwah, NJ) by centrifugation (4,696 × *g*, 4°C, 20 min) in a swing-out bucket rotor. Spent medium was decanted in an anaerobic chamber, and the cell pellet was resuspended in sterile and anoxic Fe/S-free base salts medium. All experiments used washed *M. voltae* cells, grown with 26 μM Fe(II) and 2 mM HS<sup>-</sup>, as the inoculum (10% [vol/vol]). After inoculation, the headspace of microcosm assays was flushed with an 80:20 (vol/vol) mixture of N<sub>2</sub>-CO<sub>2</sub> gas that had been passed through a 0.2-μm filter for at least 15 min. Finally, the culture bottles were pressurized to 3.21 or 1.65 atm for 165-ml and 2-liter reactors, respectively, inoculated, and incubated at 38°C in the dark and statically on their sides to minimize disruption of microbe-mineral interactions while maximizing gas diffusion.

**Measurement of activity and growth.** Headspace gas from cultures was sampled with a N<sub>2</sub>-flushed syringe equipped with a stopcock and needle and were diluted with ultra-high purity N<sub>2</sub> into CaliBond bags (Calibrated Instruments Inc., Manhasset, NY) prior to CH<sub>4</sub> determination. CH<sub>4</sub> was determined by gas chromatography by injecting 5 ml of sample into an injector valve set at 55°C on a SRI 8610C gas chromatograph (SRI Instruments, Torrance, CA) equipped with a 4.5-m by 0.125-in. (outside diameter) Hayesep DB 100/120 packed column with the oven set to 44°C (Valco Instrument Company Inc., Houston, TX). CH<sub>4</sub> was detected by a flame ionization detector set at 156°C with ultra-high-purity He as the carrier gas. CH<sub>4</sub> peak area values were converted to parts per million using a standard curve (EGAS Depot, Nampa, ID). Dissolved HS<sup>-</sup> was determined via colorimetry (670 nm) using the methylene blue assay (75) and converted to total sulfide (dissolved and gas phase) using a standard Henry's Law solubility constant of 0.101 M·atm<sup>-1</sup> for HS<sup>-</sup> that was temperature (38°C) adjusted to 0.075 (76). Absorbance was measured using a Genesys 105 visible-spectrum (Vis) spectrophotometer (Thermo Fisher Scientific, Waltham, MA). Growth was determined by direct counting of cells using a Petroff-Hausser counting chamber on a Nikon YS100 light microscope with a 100× oil lens objective (Nikon, Tokyo, Japan). Prior to counting, an aliquot of cells was collected and concentrated by centrifugation at 15,000 × *g* for 15 min in a fixed-angle rotor.

**Culture harvesting and cell-mineral separation.** Large (800 ml in 2.0-liter bottles) cultures of *M. voltae* were used for AA and EPR analyses. Cultures were monitored for cells as described above and were harvested at mid-log phase after cultures had reached a density of >10<sup>8</sup> cells ml<sup>-1</sup>. Biomass was concentrated anaerobically from 800 ml of cultures via centrifugation (15,000 × *g*, 4°C, 60 min) in a Sorvall RC-5B centrifuge with a fixed-angle GSA rotor (DuPont Instruments, Wilmington, DE) and 250-ml centrifuge bottles equipped with gas-tight seals (Nalgene Nunc International, Rochester, NY). After centrifugation, the bottles were transferred back to the anaerobic chamber and the supernatant was carefully decanted. The pellets in each bottle were resuspended and then recombined in 50 ml of sterile and anoxic Fe/S-free base salts medium. The 50-ml concentrate was then further centrifuged (4,696 × *g*, 4°C, 60 min) in a swing-out bucket rotor, and the supernatant was carefully decanted. The pellet was then further processed for cell separation (see below) for use in AA or EPR.

Our previous observations indicated that cells grown with FeS<sub>2</sub> preferentially associate with the mineral (26). We therefore developed and tested a protocol to separate cells from FeS<sub>2</sub>. To achieve this, we took a pellet from an 800-ml culture and resuspended it in 8 ml of sterile and anoxic Fe/S-free base salts medium. The cell concentrate was then poured into a 15-ml centrifuge tube (Globe Scientific). Percoll (GE Healthcare, Chicago, IL) was prepared according to the manufacturer's directions and was adjusted to 0.4 M NaCl. The Percoll working solution was then sparged with 0.2-μm-filtered N<sub>2</sub> via a canula and vent needle for 45 min per 100 ml aliquot in a sealed glass serum bottle. The solution was then brought into the anaerobic chamber, and 4 ml was slowly underlaid beneath the cell concentrate by addition via a sterile cannula and syringe. Cells were first separated from bulk mineral by a slow spin at 1,000 × *g* for 10 min at 4°C in a swing-out bucket rotor. The samples were then removed and returned to the anaerobic chamber. A pipette was then used to extract the cell fraction that overlay the Percoll (~8.5 ml of cell extract and minor amounts of Percoll) and was transferred to a fresh 50-ml centrifuge tube. Sterile and anoxic Fe/S-free base salts medium was then added to increase the volume to 40 ml. The tubes and their contents were mixed by mild vortexing, and the cells were concentrated by centrifugation (4,696 × *g*, 4°C, 30 min). In the anaerobic chamber, the supernatant was carefully decanted, and the cells were again resuspended in 8 ml of sterile and anoxic Fe/S-free base salts medium and transferred to a 15-ml centrifuge tube. At this point, 1 ml of an anoxic, filter-sterilized detergent solution containing 0.02% Tween 80, 0.4 M NaCl, 20% methanol, 20 mM EDTA, and 20 mM sodium pyrophosphate was added (modified from reference 77). The sample was then vortexed for 10 s to mildly disrupt any cell/mineral interactions while attempting to keep whole cells intact. As before, 4 ml of Percoll working solution was added under the sample, and the cells were subjected to a second round of centrifugation (2,000 × *g*, 4°C, 20 min).

The cells were extracted with a pipette, transferred to a clean 50-ml centrifuge tube, and washed in 40 ml of basal medium. The resulting cell pellet was then used for AA and EPR spectroscopic analyses (see below).

The efficacy of the cell separation protocol was examined using 800 ml culture of *M. voltae* grown on  $\text{Fe(II)/HS}^-$ . Cell biomass was concentrated by centrifugation, as described above, and the cell pellet was resuspended in 9 ml of anoxic base salts medium. Triplicate 3-ml aliquots of the cells were dispensed into 15-ml centrifuge tubes containing 1 ml of base salts medium (control) or 1 ml base salts medium amended with  $\text{FeS}_2$ . The amount of  $\text{FeS}_2$  added was the amount that would have been present in a culture of equivalent volume. The volume of each sample was then increased to 8 ml using anoxic base salts medium. These samples were then separated from the added minerals as described above, and the cell density of the extract was determined via direct counting as described above. The remainder of the cells were pelleted and processed for AA analysis (see below).

**Sample preparation for AA and EPR spectroscopy.** Washed cell pellets from 800 ml cultures were resuspended in 2.5 ml of anoxic base salts medium using a pipette. Once pellets were fully resuspended, 2,000  $\mu\text{l}$ , 500  $\mu\text{l}$ , and 10  $\mu\text{l}$  of the cell suspension were subsampled for EPR spectroscopy, AA spectroscopy, and cell density determination, respectively. Samples for EPR and AA spectroscopic analyses were placed into 2.0- or 1.5-ml screw-cap microcentrifuge tubes with O-ring fittings, respectively (Thermo Fisher Scientific). The tubes and their contents were then centrifuged in a fixed-angle rotor at  $15,000 \times g$  for 15 min at  $4^\circ\text{C}$ . The samples for cell counts were diluted 40-fold and subjected to cell counting immediately. After centrifugation, the supernatant of the samples for use in EPR and AA spectroscopy was removed from the cell pellet using a pipette. Cell pellets for determination of Fe content via AA spectroscopy were stored at  $-80^\circ\text{C}$ , while those for EPR spectroscopy were resuspended in 300  $\mu\text{l}$  of anoxic base salts medium containing 25% glycerol as a glassing agent. Samples for EPR spectroscopy were transferred into EPR tubes (4-mm OD; Wilmad Lab Glass, NJ, USA), capped with rubber septa, and then immediately removed from the chamber and flash frozen in liquid  $\text{N}_2$ . Tubes and their contents were stored at liquid  $\text{N}_2$  temperatures until spectral acquisition occurred.

**AA spectroscopy.** Frozen cell pellets for AA spectroscopic analysis were thawed at room temperature ( $\sim 21^\circ\text{C}$ ), and then 750  $\mu\text{l}$  of 10% trace metal-free nitric acid was added to the samples. The tubes were sealed, and the pellets were resuspended by gentle pipetting and mild vortexing. The tubes were then incubated for 36 h at  $98^\circ\text{C}$  in a Isotemp heat block (Thermo Fisher Scientific). The tubes were checked approximately every 12 h and were vortexed to encourage digestion. Once the samples had fully digested, the samples were diluted with 0.75 ml MQ  $\text{H}_2\text{O}$  and were again mixed by mild vortexing. Using a 0.2- $\mu\text{m}$  PTFE syringe filter that had been prerinsed with 5 ml of MQ  $\text{H}_2\text{O}$ , the samples were filtered into sterile 2.0-ml microcentrifuge tubes. The samples were then analyzed by flame AA spectroscopy using an Agilent 240 FS instrument (Agilent Technologies Inc., Santa Clara, CA) equipped with an Fe lamp utilizing an acetylene/air mixture (11:60  $\text{lb/in}^2$  partial pressures) as a fuel source.

The Fe content for the samples was determined using a standard curve prepared from a 1,000-ppm Fe standard (Ricca Chemical Company, Arlington, TX). All dilutions and standards were prepared in fresh 5% nitric acid. The Fe content for each sample was then used to determine the amount of Fe on a per-cell basis, which was ultimately normalized to cell volume as determined with TEM.

**EPR spectroscopy.** Low-temperature, continuous-wave (CW), X-band (9.38 GHz) EPR spectra were collected using a Bruker EMX spectrometer fitted with a ColdEdge (Sumitomo Cryogenics) 10 K waveguide in-cavity cryogen-free system, a helium Stinger recirculating unit (Sumitomo Cryogenics, ColdEdge Technologies, Allentown, PA), and an Oxford Mercury iTC controller unit. For measurements below 75 K, helium gas flow was maintained at 100  $\text{lb/in}^2$ ; higher-temperature measurements required decreased supply pressure. Unless otherwise noted, the typical spectral parameters were as follows: microwave power, 5.3 mW; modulation frequency, 100 kHz; and modulation amplitude, 10 G. All spectral data were plotted in the OriginPro software program (2018b; OriginLab Corp. Northampton, MA, USA). EPR spin quantitation was accomplished via double integration of  $S = 1/2$  [Fe-S] cluster signals and comparison to a 100  $\mu\text{M}$  copper(II) triethanolamine spin standard under nonsaturating conditions, according to the method of Aasa and Vänngård (78).

**Protein extraction, quantification, and digestion.** Prior to extracting protein from samples, a control experiment was conducted to determine potential effects of  $\text{FeS}_2$  on protein extraction and recovery. An 800-ml culture of *M. voltae* grown with  $\text{Fe(II)/HS}^-$  was concentrated via centrifugation as described above. The concentrated pellet was resuspended in 7 ml of anoxic base salts medium, and six 1.0-ml aliquots were dispersed into sterile 2.0-ml microcentrifuge tubes. Three tubes were amended with 0.0175 g  $\text{FeS}_2$  and three received no added  $\text{FeS}_2$ . This is the amount of  $\text{FeS}_2$  that would be added to a 75-ml culture. The tubes were mixed by inversion and 30 s of mild vortexing and were then subjected to centrifugation ( $15,000 \times g$ ,  $4^\circ\text{C}$ , 15 min). The supernatant was carefully discarded, and the cell pellet and any added  $\text{FeS}_2$  were frozen at  $-80^\circ\text{C}$  until analysis. The cells were then digested as described above, 40  $\mu\text{g}$  of protein extract was analyzed by SDS-PAGE, and a subsample was quantified with a NanoDrop spectrophotometer (Thermo Scientific, San Jose, CA). For SDS-PAGE analyses, aliquots of protein were combined with Laemmli buffer (Bio-Rad, Hercules, CA), and 40  $\mu\text{g}$  of protein was loaded to each lane of a 4 to 20% Mini-Protean TGX precast gel (Bio-Rad). Gel electrophoresis was performed at 150 V for approximately 45 min using SDS buffer. There was no discernible difference in the amount of protein recovered (Bradford assay and NanoDrop spectrometry) or the banding pattern of proteins on an SDS-PAGE gel in cell pellets incubated in the presence or absence of  $\text{FeS}_2$  (Fig. S7). Thus, steps were not used to remove  $\text{FeS}_2$  from cultures prior to subsequent protein extraction for proteomics analyses.

For proteomics analyses, 75-ml cultures of *M. voltae* were grown in 165-ml serum bottles that were harvested during mid-log phase of growth. The entirety of the cultures was harvested anaerobically

within an anaerobic chamber by transferring cultures into 50-ml centrifuge tubes (Globe Scientific) that were centrifuged at  $4,696 \times g$  for 20 min at 4°C in a swing-out bucket rotor. Pellets from the same sample were combined and then re-centrifuged as above. The supernatant was then carefully decanted, and the pellets were immediately placed at  $-80^{\circ}\text{C}$ .

Phosphate-buffered saline (PBS [pH 7.0]; 137 mM NaCl, 2.7 mM KCl, 10 mM  $\text{Na}_2\text{HPO}_4$ , and 1.8 mM  $\text{KH}_2\text{PO}_4$ ) containing protease inhibitor (complete mini-EDTA-free protease inhibitor cocktail; Roche) was used to resuspend cell pellets for protein extraction. The cells were suspended in PBS, placed on ice, and sonicated for 15 min using a Biologix ultrasonic homogenizer 3000 using 10 pulses at 100 W and 2 kHz each for 3 s, after which samples were subjected to centrifugation ( $10,000 \times g$  for 30 min at 4°C) to pellet cell debris. Prechilled ( $-80^{\circ}\text{C}$ ) acetone was added to the samples, which were then incubated at  $-80^{\circ}\text{C}$  for 1 h and then at  $-20^{\circ}\text{C}$  for 12 h to precipitate protein. Samples were centrifuged to pellet protein at  $10,000 \times g$  for 20 min at 4°C. The supernatant was carefully decanted, leaving the protein pellet, which was stored at  $-80^{\circ}\text{C}$  until subjected to digestion.

Protein digestion was performed at the University of Nevada, Reno Proteomics Center using the EasyPep mini-MS sample prep kit (Thermo Scientific, San Jose, CA). During the digestion, the samples were briefly subjected to reduction and alkylation using iodoacetamide, and then samples were digested using a trypsin-LysC mixture (modified from the work of Lundby et al. [79]). Samples were passed over a  $\text{C}_{18}$  reverse-phase column prior to liquid chromatography-mass spectrometry (LC-MS) to remove undigested protein. Protein digests were separated by LC with an UltiMate 3000 RSLCnano system (Thermo Scientific) with a self-packed ReproSil-Pur  $\text{C}_{18}$  column (100  $\mu\text{m}$  by 35 cm). The column was packed at  $9,000 \text{ lb/in}^2$  using a nano-LC column packing kit (nanoLCMS; Gold River, CA). Chromatography was performed using a 92-min method with a 2-to-90% gradient of solvent B (0.1% formic acid in acetonitrile) and solvent A (0.1% formic acid in water). Using a digital Pico View nanospray source (New Objectives, Woburn, MA), the LC was coupled to the MS, which had an ABIRD background suppressor (ESI Source Solutions, Woburn, MA). Data-independent acquisition and MS analysis were performed using an Orbitrap Fusion MS (Thermo Scientific). To generate a reference library, 6 gas phase fractions (GPF) of the biological samples were pooled. Acquisition was performed using 4  $m/z$  precursor isolation windows in a staggered pattern (GPF1, 398.4 to 502.5  $m/z$ ; GPF2, 498.5 to 602.5  $m/z$ ; GPF3, 598.5 to 702.6  $m/z$ ; GPF4, 698.6 to 802.6  $m/z$ ; GPF5, 798.6 to 902.7  $m/z$ ; GPF6, 898.7 to 1,002.7  $m/z$ ). Individual biological samples were run on the same gradient as the GPFs using a staggered window scheme (4  $m/z$  Exploris 480; 24  $m/z$  Fusion) and mass range of 385 to 1,015  $m/z$ .

**Proteomics data and statistical analysis.** Protein fragments and retention times were identified with ScaffoldDIA (2.1.0). An empirically corrected library combining GPF and the deep neural network ProSight (80) were used to generate predicted fragments and retention times of peptides (Proteome Software, Portland, OR). Using ScaffoldDIA (2.1.0), data files were converted to mzML file format (81) using ProteoWizard (3.0.19254), and then staggered window deconvolution and alignment based on retention times were performed. The data were then individually searched against the empirically corrected library built from UniProt and Scaffold using a peptide mass tolerance of 10.0 ppm and a fragment mass tolerance of 10.0 ppm. Variable carbamidomethylation modifications to cysteine were considered. A maximum of 1 missed cleavage site by the trypsin enzyme served as the cutoff for peptide matching. Only peptides with 2 to 3 charges and 6 to 30 amino acids in length were considered. Identified peptides were assigned posterior error probabilities and filtered by Percolator (3.01.nightly-13-655e4c7-dirty) (82–84) to achieve a maximum false discovery rate (FDR) of 0.01. Quantification of peptides using Encyclopedia (0.9.2) was performed by selecting the 5 highest-quality fragment ions. To satisfy the principles of parsimony, proteins that contained similar peptides and could not be distinguished based on LC-MS analysis were assumed to be a single protein and were combined. Proteins were identified with at least 2 peptides, which achieved a protein FDR threshold of 1.0%.

Individual protein intensities returned from ScaffoldDIA (2.1.0) were  $\log_{10}$  transformed and normalized using the Scaffold method.  $t$  tests were performed, and fold changes were calculated for differential comparisons of proteins after sum normalization using MetabolAnalyst (R version 3.6.3) (85). [Fe-S]-binding proteins were predicted from the *M. voltae* strain A3 proteome (downloaded from UniProt on 20 July 2020) using the online server MetalPredator (61).

**Transmission electron microscopy.** Cells of *M. voltae* were grown to mid-log phase in 2-liter reactors with either  $\text{Fe(II)/HS}^-$  or  $\text{FeS}_2$ , as described above. The cells were then subjected to the cell separation procedure described above; however, no detergent was added to samples in an attempt to maintain cell surface integrity. After the separation procedure, cells were fixed overnight ( $\sim 12$  h) at 4°C in 2.5% EM-grade glutaraldehyde (Electron Microscopy Sciences, Hatfield, PA) in 0.1 M potassium sodium phosphate buffer. After fixation, the cells were washed three times in MQ  $\text{H}_2\text{O}$  and then incubated with 2% osmium tetroxide for 4 h at room temperature ( $\sim 21^{\circ}\text{C}$ ). The fixed cells were then rinsed twice with MQ  $\text{H}_2\text{O}$  and subjected to an ethanol dehydration series (50% to 100% molecular grade ethanol). After dehydration, the fixed and dehydrated cells were incubated twice for 10 min each in 100% propylene oxide (PO). The cells were then incubated overnight ( $\sim 12$  h) at 4°C with 2:1 PO to Spurr's embedding resin mixture. This process was repeated with cells suspended in 1:2 PO to Spurr's, followed by 100% Spurr's. Prior to loading into BEEM capsules (Ted Pella Inc., Redding, CA), cells in Spurr's were brought to room temperature ( $\sim 21^{\circ}\text{C}$ ) and then centrifuged briefly to concentrate the cells. The concentrated cell pellet was transferred to a BEEM capsule and cured at  $70^{\circ}\text{C}$  overnight ( $\sim 12$  h) before thin sectioning. BEEM capsules were then removed, and the sample was thin sectioned with a diamond knife on a Reichert ultramicrotome (Leica Microsystems Inc., Buffalo Grove, IL). Sections close to 60 nm thick were placed on 300 mesh copper grids (Ted Pella) and then stained with uranyl acetate and Reynold's lead citrate. Grids were viewed with a LEO 912 transmission electron microscope (Zeiss, Oberkochen, Germany)

operated at an accelerating voltage of 100 kV, and pictures were taken with a 2k-by-2k Proscan camera. Perpendicular measurements of cell diameter were manually performed on the instrument.

**Data availability.** Raw and processed proteome data have been deposited in the ProteomeXchange Consortium via the PRIDE (86) partner repository with the data set identifier PXD024933.

## SUPPLEMENTAL MATERIAL

Supplemental material is available online only.

**SUPPLEMENTAL FILE 1**, PDF file, 0.7 MB.

**SUPPLEMENTAL FILE 2**, XLSX file, 0.02 MB.

## ACKNOWLEDGMENTS

This work was supported by the Division of Chemical Sciences, Geosciences, and Biosciences, Office of Basic Energy Sciences of the U.S. Department of Energy through grant DE-SC0020246 to E.M.S., B.B., J.B.B., and E.S.B.

## REFERENCES

1. Thauer RK, Kaster A-K, Seedorf H, Buckel W, Hedderich R. 2008. Methanogenic archaea: ecologically relevant differences in energy conservation. *Nat Rev Microbiol* 6:579–591. <https://doi.org/10.1038/nrmicro1931>.
2. Enzmann F, Mayer F, Rother M, Holtmann D. 2018. Methanogens: biochemical background and biotechnological applications. *AMB Express* 8:1–1. <https://doi.org/10.1186/s13568-017-0531-x>.
3. Beinert H, Holm RH, Munck E. 1997. Iron-sulfur clusters: nature's modular, multipurpose structures. *Science* 277:653–659. <https://doi.org/10.1126/science.277.5326.653>.
4. Johnson DC, Dean DR, Smith AD, Johnson MK. 2005. Structure, function, and formation of biological iron-sulfur clusters. *Annu Rev Biochem* 74:247–281. <https://doi.org/10.1146/annurev.biochem.74.082803.133518>.
5. Thauer RK, Kaster AK, Goenrich M, Schick M, Hiromoto T, Shima S. 2010. Hydrogenases from methanogenic archaea, nickel, a novel cofactor, and H<sub>2</sub> storage. *Annu Rev Biochem* 79:507–536. <https://doi.org/10.1146/annurev.biochem.030508.152103>.
6. Leigh JA. 2000. Nitrogen fixation in methanogens: the archaeal perspective. *Curr Issues Mol Biol* 2:125–131.
7. Ragsdale SW, Kumar M. 1996. Nickel-containing carbon monoxide dehydrogenase/acetyl-CoA synthase. *Chem Rev* 96:2515–2540. <https://doi.org/10.1021/cr950058+>.
8. Johnson C, England A, Munro-Ehrlich R, Colman DR, DuBois JL, Boyd ES. 2021. Pathways of iron and sulfur acquisition, cofactor assembly, destination, and storage in diverse archaeal methanogens, methanotrophs, and alkano-trophs. *J Bacteriol* <https://doi.org/10.1128/JB.00117-21>. Epub ahead of print.
9. Liu Y, Sieprawska-Lupa M, Whitman WB, White RH. 2010. Cysteine is not the sulfur source for iron-sulfur cluster and methionine biosynthesis in the methanogenic archaeon *Methanococcus maripaludis*. *J Biol Chem* 285:31923–31929. <https://doi.org/10.1074/jbc.M110.152447>.
10. Major TA, Burd H, Whitman WB. 2004. Abundance of 4Fe-4S motifs in the genomes of methanogens and other prokaryotes. *FEMS Microbiol Lett* 239:117–123. <https://doi.org/10.1016/j.femsle.2004.08.027>.
11. Liu Y, Beer LL, Whitman WB. 2012. Methanogens: a window into ancient sulfur metabolism. *Trends Microbiol* 20:251–258. <https://doi.org/10.1016/j.tim.2012.02.002>.
12. Wolfe JM, Fournier GP. 2018. Horizontal gene transfer constrains the timing of methanogen evolution. *Nat Ecol Evol* 2:897–903. <https://doi.org/10.1038/s41559-018-0513-7>.
13. Paulo LM, Stams AJM, Sousa DZ. 2015. Methanogens, sulphate and heavy metals: a complex system. *Rev Environ Sci Biotechnol* 14:537–553. <https://doi.org/10.1007/s11157-015-9387-1>.
14. Luther GW, Rickard DT. 2005. Metal sulfide cluster complexes and their biogeochemical importance in the environment. *J Nanopart Res* 7:389–407. <https://doi.org/10.1007/s11051-005-4272-4>.
15. Rickard D, Luther GW. 2007. Chemistry of iron sulfides. *Chem Rev* 107:514–562. <https://doi.org/10.1021/cr0503658>.
16. Berner RA. 1969. The synthesis of framboidal pyrite. *Econ Geol* 64:383–384. <https://doi.org/10.2113/gsecongeo.64.4.383>.
17. Berner RA. 1984. Sedimentary pyrite formation: an update. *Geochim Cosmochim Acta* 48:605–615. [https://doi.org/10.1016/0016-7037\(84\)90089-9](https://doi.org/10.1016/0016-7037(84)90089-9).
18. Luther GW, Glazer BT, Ma S, Trouwborst RE, Moore TS, Metzger E, Kraiya C, Waite TJ, Druschel G, Sundby B, Tallefert M, Nuzzio DB, Shank TM, Lewis BL, Brendel PJ. 2008. Use of voltammetric solid-state (micro)electrodes for studying biogeochemical processes: laboratory measurements to real time measurements with an *in situ* electrochemical analyzer (ISEA). *Mar Chem* 108:221–235. <https://doi.org/10.1016/j.marchem.2007.03.002>.
19. Luther GW, Rozan TF, Tallefert M, Nuzzio DB, Di Meo C, Shank TM, Lutz RA, Cary SC. 2001. Chemical speciation drives hydrothermal vent ecology. *Nature* 410:813–816. <https://doi.org/10.1038/35071069>.
20. Drobner E, Huber H, Wächtershäuser G, Rose D, Stetter KO. 1990. Pyrite formation linked with hydrogen evolution under anaerobic conditions. *Nature* 346:742–744. <https://doi.org/10.1038/346742a0>.
21. Rickard D. 1997. Kinetics of pyrite formation by the H<sub>2</sub>S oxidation of iron (II) monosulfide in aqueous solutions between 25 and 125°C: the rate equation. *Geochim Cosmochim Acta* 61:115–134. [https://doi.org/10.1016/S0016-7037\(96\)00321-3](https://doi.org/10.1016/S0016-7037(96)00321-3).
22. Wolthers M, Charlet L, van Der Linde PR, Rickard D, van Der Weijden CH. 2005. Surface chemistry of disordered mackinawite (FeS). *Geochim Cosmochim Acta* 69:3469–3481. <https://doi.org/10.1016/j.gca.2005.01.027>.
23. Bapteste E, Brochier C, Boucher Y. 2005. Higher-level classification of the Archaea: evolution of methanogenesis and methanogens. *Archaea* 1:353–363. <https://doi.org/10.1155/2005/859728>.
24. Petitjean C, Deschamps P, Lopez-Garcia P, Moreira D, Brochier-Armanet C. 2015. Extending the conserved phylogenetic core of archaea disentangles the evolution of the third domain of life. *Mol Biol Evol* 32:1242–1254. <https://doi.org/10.1093/molbev/msv015>.
25. Brochier-Armanet C, Forterre P, Gribaldo S. 2011. Phylogeny and evolution of the Archaea: one hundred genomes later. *Curr Opin Microbiol* 14:274–281. <https://doi.org/10.1016/j.mib.2011.04.015>.
26. Payne D, Spietz RL, Boyd ES. 2021. Reductive dissolution of pyrite by methanogenic Archaea. *ISME J* <https://doi.org/10.1038/s41396-021-01028-3>. Epub ahead of print.
27. Truche L, Berger G, Destigneville C, Guillaume D, Giffaut E. 2010. Kinetics of pyrite to pyrrhotite reduction by hydrogen in calcite buffered solutions between 90 and 180°C: implications for nuclear waste disposal. *Geochim Cosmochim Acta* 74:2894–2914. <https://doi.org/10.1016/j.gca.2010.02.027>.
28. Scherer P, Sahm H. 1981. Influence of sulphur-containing compounds on the growth of *Methanosarcina barkeri* in a defined medium. *Eur J Appl Microbiol Biotechnol* 12:28–35. <https://doi.org/10.1007/BF00508115>.
29. Sargent MG. 1975. Control of cell length in *Bacillus subtilis*. *J Bacteriol* 123:7–19. <https://doi.org/10.1128/jb.123.1.7-19.1975>.
30. Schaechter M, Maaløe O, Kjeldgaard NO. 1958. Dependency on medium and temperature of cell size and chemical composition during balanced growth of *Salmonella typhimurium*. *J Gen Microbiol* 19:592–606. <https://doi.org/10.1099/00221287-19-3-592>.
31. Pierucci O. 1978. Dimensions of *Escherichia coli* at various growth rates: model for envelope growth. *J Bacteriol* 135:559–574. <https://doi.org/10.1128/jb.135.2.559-574.1978>.
32. Vadia S, Levin PA. 2015. Growth rate and cell size: a re-examination of the growth law. *Curr Opin Microbiol* 24:96–103. <https://doi.org/10.1016/j.mib.2015.01.011>.
33. Merchant SS, Helmann JD. 2012. Elemental economy: microbial strategies for optimizing growth in the face of nutrient limitation. *Adv Microbiol Phys* 60:91–210. <https://doi.org/10.1016/B978-0-12-398264-3.00002-4>.

34. Posey JE, Gherardini FC. 2000. Lack of a role for iron in the Lyme disease pathogen. *Science* 288:1651–1653. <https://doi.org/10.1126/science.288.5471.1651>.
35. Chien YT, Auerbuch V, Brabban AD, Zinder SH. 2000. Analysis of genes encoding an alternative nitrogenase in the archaeon *Methanosarcina barkeri* 227. *J Bacteriol* 182:3247–3253. <https://doi.org/10.1128/JB.182.11.3247-3253.2000>.
36. Jasniowski AJ, Lee CC, Ribbe MW, Hu Y. 2020. Reactivity, mechanism, and assembly of the alternative nitrogenases. *Chem Rev* 120:5107–5157. <https://doi.org/10.1021/acs.chemrev.9b00704>.
37. Joerger RD, Bishop PE. 1988. Bacterial alternative nitrogen fixation systems. *Crit Rev Microbiol* 16:1–14. <https://doi.org/10.3109/10408418809104465>.
38. Rohlin L, Gunsalus RP. 2010. Carbon-dependent control of electron transfer and central carbon pathway genes for methane biosynthesis in the Archaeon, *Methanosarcina acetivorans* strain C2A. *BMC Microbiol* 10:62–62. <https://doi.org/10.1186/1471-2180-10-62>.
39. Afting C, Kremmer E, Brucker C, Hochheimer A, Thauer RK. 2000. Regulation of the synthesis of H<sub>2</sub>-forming methylenetetrahydromethanopterin dehydrogenase (Hmd) and of HmdII and HmdIII in *Methanothermobacter marburgensis*. *Arch Microbiol* 174:225–232. <https://doi.org/10.1007/s002030000197>.
40. Shima S, Pilak O, Vogt S, Schick M, Stagni MS, Meyer-Klaucke W, Warkentin E, Thauer RK, Ermiler U. 2008. The crystal structure of [Fe]-hydrogenase reveals the geometry of the active site. *Science* 321:572–575. <https://doi.org/10.1126/science.1158978>.
41. Rupp H, Rao KK, Hall DO, Cammack R. 1978. Electron spin relaxation of iron-sulphur proteins studied by microwave power saturation. *Biochim Biophys Acta* 537:255–269. [https://doi.org/10.1016/0005-2795\(78\)90509-3](https://doi.org/10.1016/0005-2795(78)90509-3).
42. Bertrand P, Gayda JP, Rao KK. 1982. Electron spin-lattice relaxation of the 4Fe-4S ferredoxin from *Bacillus stearothermophilus*. Comparison with other iron proteins. *J Chem Phys* 76:4715–4719. <https://doi.org/10.1063/1.442788>.
43. Shepard EM, Byer AS, Aggarwal P, Betz JN, Scott AG, Shisler KA, Usselman RJ, Eaton GR, Eaton SS, Broderick JB. 2017. Electron spin relaxation and biochemical characterization of the hydrogenase maturase HydF: insights into [2Fe-2S] and [4Fe-4S] cluster communication and hydrogenase activation. *Biochemistry* 56:3234–3247. <https://doi.org/10.1021/acs.biochem.7b00169>.
44. Duin EC, Lafferty ME, Crouse BR, Allen RM, Sanyal I, Flint DH, Johnson MK. 1997. [2Fe-2S] to [4Fe-4S] cluster conversion in *Escherichia coli* biotin synthase. *Biochemistry* 36:11811–11820. <https://doi.org/10.1021/bi9706430>.
45. Broderick JB, Duffus BR, Duschene KS, Shepard EM. 2014. Radical S-adenosylmethionine enzymes. *Chem Rev* 114:4229–4317. <https://doi.org/10.1021/cr4004709>.
46. Werth MT, Kurtz DM, Howes BD, Huynh BH. 1989. Observation of S = 2 EPR signals from ferrous iron thiolate complexes—relevance to rubredoxin-type sites in proteins. *Inorg Chem* 28:1357–1361. <https://doi.org/10.1021/ic00306a028>.
47. Conover RC, Kowal AT, Fu WG, Park JB, Aono S, Adams MW, Johnson MK. 1990. Spectroscopic characterization of the novel iron-sulfur cluster in *Pyrococcus furiosus* ferredoxin. *J Biol Chem* 265:8533–8541. [https://doi.org/10.1016/S0021-9258\(19\)38921-5](https://doi.org/10.1016/S0021-9258(19)38921-5).
48. Zambrano IC, Kowal AT, Mortenson LE, Adams MW, Johnson MK. 1989. Magnetic circular dichroism and electron paramagnetic resonance studies of hydrogenases I and II from *Clostridium pasteurianum*. *J Biol Chem* 264:20974–20983. [https://doi.org/10.1016/S0021-9258\(19\)30032-8](https://doi.org/10.1016/S0021-9258(19)30032-8).
49. Lindahl PA, Day EP, Kent TA, Orme-Johnson WH, Munck E. 1985. Mossbauer, EPR, and magnetization studies of the *Azotobacter vinelandii* Fe protein. Evidence for a [4Fe-4S]<sup>1+</sup> cluster with spin S = 3/2. *J Biol Chem* 260:11160–11173. [https://doi.org/10.1016/S0021-9258\(17\)39160-3](https://doi.org/10.1016/S0021-9258(17)39160-3).
50. Ellefson WL, Wolfe RS. 1981. Component C of the methylreductase system of *Methanobacterium*. *J Biol Chem* 256:4259–4262. [https://doi.org/10.1016/S0021-9258\(19\)69427-5](https://doi.org/10.1016/S0021-9258(19)69427-5).
51. Duin EC, Prakash D, Brungess C. 2011. Methyl-coenzyme M reductase from *Methanothermobacter marburgensis*. *Methods Enzymol* 494:159–187. <https://doi.org/10.1016/B978-0-12-385112-3.00009-3>.
52. Madadi-Kahkesh S, Duin EC, Heim S, Albracht SP, Johnson MK, Hedderich R. 2001. A paramagnetic species with unique EPR characteristics in the active site of heterodisulfide reductase from methanogenic archaea. *Eur J Biochem* 268:2566–2577. <https://doi.org/10.1046/j.1432-1327.2001.02141.x>.
53. Wagner T, Koch J, Ermiler U, Shima S. 2017. Methanogenic heterodisulfide reductase (HdrABC-MvhAGD) uses two noncubane [4Fe-4S] clusters for reduction. *Science* 357:699–703. <https://doi.org/10.1126/science.aan0425>.
54. Wagner T, Ermiler U, Shima S. 2016. The methanogenic CO<sub>2</sub> reducing-and-fixing enzyme is bifunctional and contains 46 [4Fe-4S] clusters. *Science* 354:114–117. <https://doi.org/10.1126/science.aaf9284>.
55. Bertram PA, Karrasch M, Schmitz RA, Bocher R, Albracht SP, Thauer RK. 1994. Formylmethanofuran dehydrogenases from methanogenic Archaea. Substrate specificity, EPR properties and reversible inactivation by cyanide of the molybdenum or tungsten iron-sulfur proteins. *Eur J Biochem* 220:477–484. <https://doi.org/10.1111/j.1432-1033.1994.tb18646.x>.
56. Bertrand P, Gayda JP, Fee JA, Kuila D, Cammack R. 1987. Comparison of the spin-lattice relaxation properties of the two classes of [2Fe-2S] clusters in proteins. *Biochim Biophys Acta* 916:24–28. [https://doi.org/10.1016/0167-4838\(87\)90206-8](https://doi.org/10.1016/0167-4838(87)90206-8).
57. Gayda JP, Bertrand P, Deville A, More C, Roger G, Gibson JF, Cammack R. 1979. Temperature dependence of the electronic spin-lattice relaxation time in a 2-iron-2-sulfur protein. *Biochim Biophys Acta* 581:15–26. [https://doi.org/10.1016/0005-2795\(79\)90216-2](https://doi.org/10.1016/0005-2795(79)90216-2).
58. Vaccaro BJ, Clarkson SM, Holden JF, Lee DW, Wu CH, Poole li FL, Cotelesage JHH, Hackett MJ, Mohebbi S, Sun J, Li H, Johnson MK, George GN, Adams MWW. 2017. Biological iron-sulfur storage in a thioferrate-protein nanoparticle. *Nat Commun* 8:16110. <https://doi.org/10.1038/ncomms16110>.
59. Sweeney WV, Coffman RE. 1972. Magnetic properties of potassium dithioferrate: a linear chain antiferromagnet and model compound for the exchange interactions in two-iron ferredoxins. *Biochim Biophys Acta* 286:26–35. [https://doi.org/10.1016/0304-4165\(72\)90085-2](https://doi.org/10.1016/0304-4165(72)90085-2).
60. Costa KC, Wong PM, Wang T, Lie TJ, Dodsworth JA, Swanson I, Burn JA, Hackett M, Leigh JA. 2010. Protein complexing in a methanogen suggests electron bifurcation and electron delivery from formate to heterodisulfide reductase. *Proc Natl Acad Sci U S A* 107:11050–11055. <https://doi.org/10.1073/pnas.1003653107>.
61. Valasatava Y, Rosato A, Banci L, Andreini C. 2016. MetalPredator: a web server to predict iron-sulfur cluster binding proteomes. *Bioinformatics* 32:2850–2852. <https://doi.org/10.1093/bioinformatics/btw238>.
62. Kammler M, Schön C, Hantke K. 1993. Characterization of the ferrous iron uptake system of *Escherichia coli*. *J Bacteriol* 175:6212–6219. <https://doi.org/10.1128/jb.175.19.6212-6219.1993>.
63. Cartron ML, Maddocks S, Gillingham P, Craven CJ, Andrews SC. 2006. Feo - Transport of ferrous iron into bacteria. *Biometals* 19:143–157. <https://doi.org/10.1007/s10534-006-0003-2>.
64. Kaster A-K, Goenrich M, Seedorf H, Liesegang H, Wollherr A, Gottschalk G, Thauer RK. 2011. More than 200 genes required for methane formation from H<sub>2</sub> and CO<sub>2</sub> and energy conservation are present in *Methanothermobacter marburgensis* and *Methanothermobacter thermoautotrophicus*. *Archaea* 2011:973848. <https://doi.org/10.1155/2011/973848>.
65. Guedon E, Helmann JD. 2003. Origins of metal ion selectivity in the DtxR/MntR family of metalloregulators. *Mol Microbiol* 48:495–506. <https://doi.org/10.1046/j.1365-2958.2003.03445.x>.
66. Zhu Y, Kumar S, Menon AL, Scott RA, Adams MW. 2013. Regulation of iron metabolism by *Pyrococcus furiosus*. *J Bacteriol* 195:2400–2407. <https://doi.org/10.1128/JB.02280-12>.
67. Hantke K. 2001. Iron and metal regulation in Bacteria. *Curr Opin Microbiol* 4:172–177. [https://doi.org/10.1016/s1369-5274\(00\)00184-3](https://doi.org/10.1016/s1369-5274(00)00184-3).
68. Boyd ES, Thomas KM, Dai Y, Boyd JM, Outten FW. 2014. Interplay between oxygen and Fe-S cluster biogenesis: insights from the Suf pathway. *Biochemistry* 53:5834–5847. <https://doi.org/10.1021/bi500488r>.
69. Takahashi Y, Tokumoto U. 2002. A third bacterial system for the assembly of iron-sulfur clusters with homologs in archaea and plastids. *J Biol Chem* 277:28380–28383. <https://doi.org/10.1074/jbc.C200365200>.
70. Outten FW. 2015. Recent advances in the Suf Fe-S cluster biogenesis pathway: beyond the Proteobacteria. *Biochim Biophys Acta* 1853:1464–1469. <https://doi.org/10.1016/j.bbamcr.2014.11.001>.
71. Blahut M, Sanchez E, Fisher CE, Outten FW. 2020. Fe-S cluster biogenesis by the bacterial Suf pathway. *Biochim Biophys Acta Mol Cell Res* 1867:118829. <https://doi.org/10.1016/j.bbamcr.2020.118829>.
72. Outten FW, Wood MJ, Muñoz FM, Storz G. 2003. The SufE protein and the SufBCD complex enhance SufS cysteine desulfurase activity as part of a sulfur transfer pathway for Fe-S cluster assembly in *Escherichia coli*. *J Biol Chem* 278:45713–45719. <https://doi.org/10.1074/jbc.M308004200>.
73. Whitman WB, Ankwarda E, Wolfe RS. 1982. Nutrition and carbon metabolism of *Methanococcus voltae*. *J Bacteriol* 149:852–863. <https://doi.org/10.1128/jb.149.3.852-863.1982>.
74. Sauerwald A, Zhu W, Major TA, Roy H, Palioura S, Jahn D, Whitman WB, Yates JR, III, Ibbas M, Söll D. 2005. RNA-dependent cysteine biosynthesis in archaea. *Science* 307:1969–1972. <https://doi.org/10.1126/science.1108329>.
75. Fogo JK, Popowsky M. 1949. Spectrophotometric determination of hydrogen sulfide. *Anal Chem* 21:732–734. <https://doi.org/10.1021/ac60030a028>.

76. Sander R. 2015. Compilation of Henry's law constants (version 4.0) for water as solvent. *Atmos Chem Phys* 15:4399–4981. <https://doi.org/10.5194/acp-15-4399-2015>.
77. Morono Y, Terada T, Kallmeyer J, Inagaki F. 2013. An improved cell separation technique for marine subsurface sediments: applications for high-throughput analysis using flow cytometry and cell sorting. *Environ Microbiol* 15:2841–2849. <https://doi.org/10.1111/1462-2920.12153>.
78. Aasa R, Vännngård T. 1975. EPR signal intensity and powder shapes: a re-examination. *J Magn Reson* 19:308–315. [https://doi.org/10.1016/0022-2364\(75\)90045-1](https://doi.org/10.1016/0022-2364(75)90045-1).
79. Lundby A, Secher A, Lage K, Nordsborg NB, Dmytriyev A, Lundby C, Olsen JV. 2012. Quantitative maps of protein phosphorylation sites across 14 different rat organs and tissues. *Nat Commun* 3:876. <https://doi.org/10.1038/ncomms1871>.
80. Searle BC, Swearingen KE, Barnes CA, Schmidt T, Gessulat S, Küster B, Wilhelm M. 2020. Generating high quality libraries for DIA MS with empirically corrected peptide predictions. *Nat Commun* 11:1548–1548. <https://doi.org/10.1038/s41467-020-15346-1>.
81. Chambers MC, Maclean B, Burke R, Amodei D, Ruderman DL, Neumann S, Gatto L, Fischer B, Pratt B, Egerton J, Hoff K, Kessner D, Tasman N, Shulman N, Frewen B, Baker TA, Brusniak MY, Paulse C, Creasy D, Flashner L, Kani K, Moulding C, Seymour SL, Nuwaysir LM, Lefebvre B, Kuhlmann F, Roark J, Rainer P, Detlev S, Hemenway T, Huhmer A, Langridge J, Connolly B, Chadick T, Holly K, Eckels J, Deutsch EW, Moritz RL, Katz JE, Agus DB, MacCoss M, Tabb DL, Mallick P. 2012. A cross-platform toolkit for mass spectrometry and proteomics. *Nat Biotechnol* 30:918–920. <https://doi.org/10.1038/nbt.2377>.
82. Käll L, Storey JD, MacCoss MJ, Noble WS. 2008. Assigning significance to peptides identified by tandem mass spectrometry using decoy databases. *J Proteome Res* 7:29–34. <https://doi.org/10.1021/pr700600n>.
83. Käll L, Storey JD, Noble WS. 2008. Non-parametric estimation of posterior error probabilities associated with peptides identified by tandem mass spectrometry. *Bioinformatics* 24:i42–i48. <https://doi.org/10.1093/bioinformatics/btn294>.
84. Noble WS, Weston J, MacCoss MJ, Canterbury JD, Käll L. 2007. Semi-supervised learning for peptide identification from shotgun proteomics datasets. *Nat Methods* 4:923–925. <https://doi.org/10.1038/nmeth1113>.
85. Pang Z, Chong J, Li S, Xia J. 2020. MetaboAnalystR 3.0: toward an optimized workflow for global metabolomics. *Metabolites* 10:186. <https://doi.org/10.3390/metabo10050186>.
86. Perez-Riverol Y, Csordas A, Bai J, Bernal-Llinares M, Hewapathirana S, Kundu DJ, Inuganti A, Griss J, Mayer G, Eisenacher M, Pérez E, Uszkoreit J, Pfeuffer J, Sachsenberg T, Yilmaz S, Tiwary S, Cox J, Audain E, Walzer M, Jarnuczak AF, Ternent T, Brazma A, Vizcaino JA. 2019. The PRIDE database and related tools and resources in 2019: improving support for quantification data. *Nucleic Acids Res* 47:D442–D450. <https://doi.org/10.1093/nar/gky1106>.